Numerical Investigation of Mechanisms Underlying Oceanic Internal Gravity Wave Power-Law Spectra

YULIN PAN

Department of Naval Architecture and Marine Engineering, University of Michigan, Ann Arbor, Michigan

BRIAN K. ARBIC AND ARIN D. NELSON

Department of Earth and Environmental Science, University of Michigan, Ann Arbor, Michigan

DIMITRIS MENEMENLIS

Jet Propulsion Laboratory, California Institute of Technology, Pasadena, California

W. R. PELTIER

Department of Physics, University of Toronto, Toronto, Ontario, Canada

WENTAO XU AND YE LI

Department of Naval Architecture and Ocean Engineering, Shanghai Jiaotong University, Shanghai, China

ABSTRACT

We consider the power-law spectra of internal gravity waves in a rotating and stratified ocean. Field measurements have shown considerable variability of spectral slopes compared to the high-wavenumber, high-frequency portion of the Garrett–Munk (GM) spectrum. Theoretical explanations have been developed through wave turbulence theory (WTT), where different power-law solutions of the kinetic equation can be found depending on the mechanisms underlying the nonlinear interactions. Mathematically, these are reflected by the convergence properties of the so-called collision integral (CL) at low- and high-frequency limits. In this work, we study the mechanisms in the formation of the power-law spectra of internal gravity waves, utilizing numerical data from the high-resolution modeling of internal waves (HRMIW) in a region northwest of Hawaii. The model captures the power-law spectra in broad ranges of space and time scales, with scalings $\omega^{-2.05\pm0.2}$ in frequency and $m^{-2.58\pm0.4}$ in vertical wavenumber. The latter clearly deviates from the GM76 spectrum but is closer to a family of induced-diffusion-dominated solutions predicted by WTT. Our analysis of nonlinear interactions is performed directly on these model outputs, which is fundamentally different from previous work assuming a GM76 spectrum. By applying a bicoherence analysis and evaluations of modal energy transfer, we show that the CL is dominated by nonlocal interactions between modes in the power-law range and low-frequency inertial motions. We further identify induced diffusion and the near-resonances at its spectral vicinity as dominating the formation of power-law spectrum.

1. Introduction

Internal gravity waves (hereafter internal waves) are ubiquitous features in a stratified ocean. Owing to their nonlinear interactions, energy supplied at large scales by atmospheric and tidal forcing is transferred to small dissipation scales, resulting in diapycnal mixing which shapes the thermodynamic balance and general circulation of the ocean (e.g., Gargett 1984; Munk and Wunsch 1998). Quantifying this energy cascade process of internal waves is a topic of long-standing interest in physical oceanography. An improved understanding of this problem is essential in the finescale parameterization for the estimation of turbulent dissipation (e.g.,

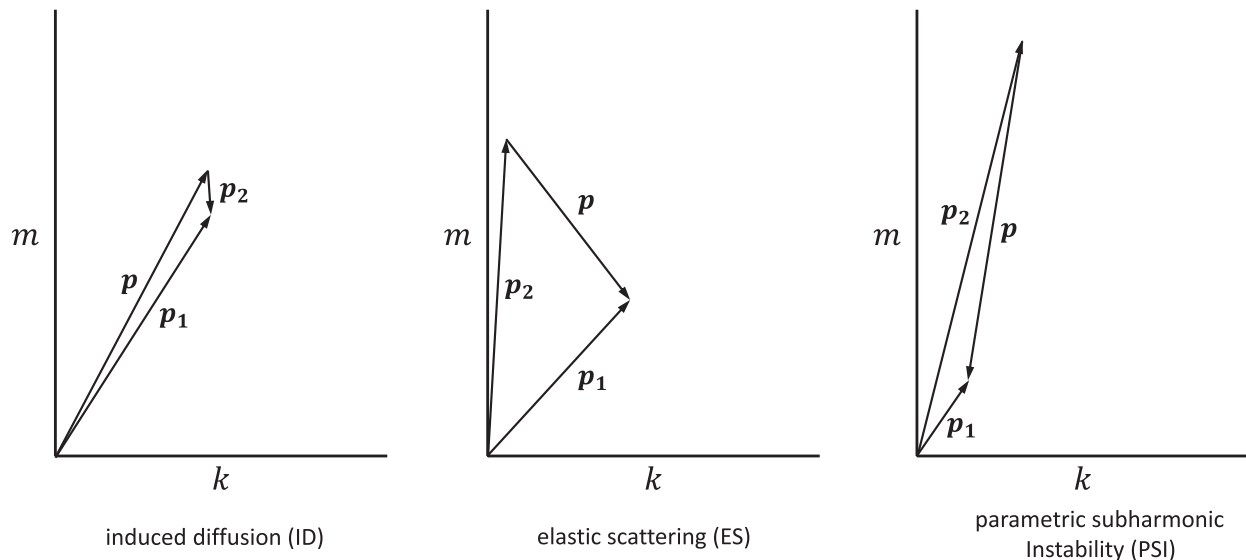*Corresponding author*: Yulin Pan, yulinpan@umich.edu

FIG. 1. Schematic plot of the induced diffusion (ID), elastic scattering (ES), and parametric subharmonic instability (PSI) for a triad $\mathbf{p}_1 = \mathbf{p} + \mathbf{p}_2$. The coordinates k and m are horizontal and vertical wavenumbers. (left) ID denotes the scattering of a high-frequency, high-wavenumber wave $\mathbf{p}$ by a low-frequency, low-wavenumber wave $\mathbf{p}_2$ into a second, nearly identical, high-frequency high-wavenumber wave $\mathbf{p}_1$. (center) ES denotes the vertical backscattering of a high-frequency wave $\mathbf{p}$ by a low-frequency wave $\mathbf{p}_2$ of twice the vertical wavenumber into a second high-frequency wave $\mathbf{p}_1$ of oppositely signed vertical wavenumber. (right) PSI denotes the decay of a low-wavenumber wave $\mathbf{p}_1$ into two high-vertical-wavenumber waves $\mathbf{p}$, $\mathbf{p}_2$ of approximately half the frequency.

Polzin et al. 2014) and the parameterization of small-scale mixing in ocean models (e.g., MacKinnon et al. 2017), both of which would potentially lead to a more comprehensive view of the ocean's role in climate.

A key factor in quantifying the energy cascade is the spectral form of the internal wave continuum covering a broad range of scales in space and time. The classical work of Garrett and Munk (Garrett and Munk 1972, 1975) employs the synthesis of observations from various types of sensors into an empirical universal wavenumber–frequency spectrum, now known as the Garrett–Munk (GM) spectrum of internal waves. One of the later revisions (Cairns and Williams 1976), resulting in the GM76 spectrum, has been found to approximate the internal wave field reasonably well. The GM76 spectrum has therefore long been considered as a standard model for the internal wave continuum, based on which the nonlinear mechanisms (e.g., energy cascade, tidal damping) are studied (e.g., McComas and Müller 1981b; Onuki and Hibiya 2018; Eden et al. 2019b; Olbers et al. 2020).

Many early theoretical efforts (e.g., Olbers 1976; McComas and Bretherton 1977; McComas and Müller 1981a,b; Müller et al. 1986) have been devoted to understanding the formation of the internal wave GM spectrum and the associated energy cascade. Of central importance to these works is the derivation of the kinetic equation (a.k.a. radiation balance equation),

an idea first developed for surface gravity waves (Hasselmann 1962; Zakharov and Filonenko 1966). The kinetic equation describes the spectral evolution as a result of the resonant nonlinear interactions of internal waves, i.e., triad interactions satisfying the wavenumber condition

$$\mathbf{p} = \mathbf{p}_1 \pm \mathbf{p}_2, \tag{1}$$

and frequency condition

$$\omega_{\mathbf{p}} = \omega_1 \pm \omega_2. \tag{2}$$

Based on the GM76 spectrum, McComas and Bretherton (1977) identify three types of scale-separated interactions (i.e., nonlocal interactions) as dominant on the resonant manifold of energy transfer, namely, the induced diffusion (ID), elastic scattering (ES), and parametric subharmonic instability (PSI). A schematic plot and physical interpretations of these mechanisms are summarized in Fig. 1. In particular, the energy transfer in the high-wavenumber, high-frequency portion of the GM spectrum is found to be dominated by the ID mechanism (McComas and Bretherton 1977; McComas and Müller 1981b).

While these earlier studies of nonlinear interactions are all based on the (assumption of) a GM spectrum, the accumulating field measurements from decades of observational programs have shown considerable

variability in the power-law spectral slopes (at the high-frequency high-wavenumber portion of the spectrum) compared to the GM spectrum (Polzin and Lvov 2011). To interpret these deviations theoretically, stationary power-law solutions of the kinetic equation can be formulated in the framework of wave turbulence theory (WTT). The recent theoretical work follows this approach with a rederivation of the kinetic equation (Lvov and Tabak 2001; Lvov et al. 2004; Lvov and Tabak 2004; Lvov et al. 2010, 2012). The derivation starts from the formulation of the dynamical equations of internal waves as a canonical Hamiltonian system in isopycnal coordinates. The kinetic equation is derived based on the Hamiltonian system under the assumption of weakly nonlinear interactions (Lvov and Tabak 2001). Lvov et al. (2010) shows that the kinetic equation yields three types of stationary power-law solutions with different spectral slopes, resulting from different mechanisms of nonlinear interactions. Mathematically, these solutions reside in different regimes depending on the properties of the so-called collision integral (CL) governing the energy transfer to a mode from a summation of resonant triad interactions. Specifically, the divergence/convergence of the integral at small or large horizontal wavenumber limits (termed infrared, IR or ultraviolet, UV limits) indicates physically the dominance of local/nonlocal interactions. The convergent, Pelinovsky–Raevsky, and ID-dominated solutions arise respectively as the integral converges at both limits, diverges at both limits with canceling singularity, and diverges at the IR limit only but regularized by the inertial frequency.

In spite of the sophistication in theory, the proposed mechanisms in the formation of internal wave power-law spectra have not been thoroughly investigated in a realistic ocean environment. The examination in realistic ocean environments is important because (i) the theory does not incorporate realistic features such as oceanic internal tides and near-inertial waves; and (ii) the kinetic equation is derived with assumptions (e.g., resonant interaction only and quasi-Gaussian statistics) which the ocean may not follow (e.g., Briscoe 1977; Lvov et al. 2012). Due to these uncertainties and the aforementioned deviations of the realistic internal wave spectrum from the GM spectrum, the mechanisms involved in the spectral formation remain elusive.

To this end, the study of nonlinear interactions using realistic ocean data is desirable. Existing work includes that of Sun and Pinkel (2012), which employs bispectral analysis to study the nonlinear triad interactions using measurements obtained from the Hawaii Ocean Mixing Experiment (HOME). The data are, however, available

only in the vertical direction and time, therefore precluding the resolution of triad interactions in three spatial dimensions. Other studies (Hibiya et al. 1998, 2002; Furue 2003; Furuichi et al. 2005; Sugiyama et al. 2009; Chen et al. 2019), based on idealized models (with periodic boundary conditions), either reduce the range of scales or confine the simulations to two spatial dimensions. Moreover, all these studies focus more on the nature of nonlinear wave interactions instead of the resulting spectral slopes, hence contribute little to the validation of WTT.

The recent development of high-resolution oceanic internal wave models [see Arbic et al. (2018) for a review] allows the internal wave dynamics to be simulated in the realistic ocean, forced by atmospheric fields and/or tides. Müller et al. (2015) show that, as the model resolution increases, the frequency spectra of internal waves in global models lie closer to the spectra computed from field measurements. This allows us to study the nonlinear interactions based on a spectrum that is spontaneously generated from tidal and wind forcing, instead of assuming a GM spectrum as in previous work. In this work, we conduct a new simulation using the Massachusetts Institute of Technology general circulation model (MITgcm; Marshall et al. 1997) with 250-m grid spacing in the horizontal direction and 264 depth layers, of a region northwest of Hawaii bounded by 24°–32°N, 193°–199°E, which is characterized by an internal tide beam (Alford et al. 2007). This regional simulation is forced at the boundaries by output from a global model that includes both atmospheric fields and the tidal potential. Such models carry low-mode near-inertial waves (e.g., Simmons and Alford 2012), and low-mode internal tides (e.g., Simmons et al. 2004; Shriver et al. 2012; Ansong et al. 2015), which are important components of the nonlocal interactions discussed later in this paper.

We analyze the (spatial and temporal) four-dimensional model outputs, with the purpose of understanding the mechanisms in the formation of the power-law spectra of internal waves. We show that the model captures the power-law wavenumber and frequency spectra in a broad range of scales (e.g., over one decade in frequency), with nontrivial deviations from the GM76 spectrum. The triad interactions that form the spectrum are first examined using bicoherence analysis, which highlights the nonlocal interactions of the modes in the high-frequency power-law range with the low-frequency near-inertial modes. We then develop the methodology required to convert the numerical data into the framework of WTT, thereby enabling the evaluation of nonlinear energy transfer governing the CL. It is found that this integral is dominated by

the interactions involving the IR-limit modes (i.e., with divergences at the IR limit but regularized by the inertial frequency). We further identify that the major mechanism dominating the energy transfer in the power-law range is indeed the ID with a finite broadening in its vicinity. All these findings are consistent with the spectral slopes obtained from the model (as predicted by the ID-dominated solutions in WTT).

This paper is organized as follows. In section 2, we briefly review the theoretical developments, focusing on the GM76 spectrum and the WTT. The interaction coefficients in the theory are rederived to ensure the correctness of our numerical implementation. In section 3, the details of the high-resolution ocean model simulation are documented. All the results including the spectral slopes, bicoherence analysis and studies in the WTT framework are presented in section 4. Further discussion and conclusions are given in section 5.

2. Review of theory

a. Garrett–Munk spectrum

The GM spectrum is an evolving concept with multiple versions. Here we review only the GM76 spectrum, which is developed after the revision (Cairns and Williams 1976). It is assumed that the spectral energy density can be represented as a separable function in vertical wavenumber m and frequency ω, i.e.,

$$E(\omega, m) = EA\left(\frac{m}{m*}\right)B(\omega),\qquad(3)$$

where $m*$ is a reference (fixed) vertical wavenumber, E is a constant representing the total energy level, and

$$A\left(\lambda \equiv \frac{m}{m*}\right) \sim (1 + \lambda^2)^{-1}, \quad B(\omega) \sim f\omega^{-1}(\omega^2 - f^2)^{-1/2},$$
$$(4)$$

with f being the inertial frequency, and with normalizations

$$\int_0^\infty A(\lambda)\,d\lambda = 1, \quad \int_f^N B(\omega)\,d\omega = 1,\qquad(5)$$

where N is the buoyancy frequency. Our focus is the power-law range (high-frequency high-wavenumber portion) of the spectrum (3), which yields

$$E(\omega) \sim \omega^{-2},\qquad(6)$$

$$E(m) \sim m^{-2},\qquad(7)$$

due to the separable functions A and B.

The spectrum $E(\omega, m)$ can be transformed to other forms involving the horizontal wavenumber $k \equiv |\mathbf{k}|$ by using relations such as $E(\omega, m)d\omega = E(k, m)dk = E(\mathbf{k}, m)d\mathbf{k} = E(k, m)2\pi k dk$ and incorporating the dispersion relation

$$\omega^2 = f^2 + N^2\left(\frac{k}{m}\right)^2.\qquad(8)$$

Of particular interest to the current work is the wave action spectrum $n(\mathbf{k}, m) \equiv E(\mathbf{k}, m)/\omega$, which can be obtained from

$$\omega n(\mathbf{k}, m)d\mathbf{k} = E(\omega, m)d\omega.\qquad(9)$$

This yields the relation

$$n(\mathbf{k}, m) \sim k^{-a}m^{-b} \Leftrightarrow E(\omega, m) \sim \omega^{2-a}m^{2-a-b}.\qquad(10)$$

For the GM76 spectrum, one can obtain $n(\mathbf{k}, m) \sim k^{-4}m^0$.

b. Wave turbulence theory of internal waves

In this section, we briefly review the derivation of the kinetic equation and the stationary spectral solution following Lvov et al. (2010). We remark that there exist different formulations of the kinetic equation (Olbers 1976; Voronovich 1979; Müller et al. 1986; Lvov et al. 2010). Formulations based on Eulerian coordinates are more appropriate than those based on isopycnal coordinates for application to the model outputs available on uniformly spaced z levels because vertical interpolation is not required. Validation of the (Eulerian-based) kinetic equation through results from spectral models of primitive equations in periodic domains has been conducted by Eden et al. (2019a, 2020). In MITgcm, however, the nonuniform z level grid makes interpolation necessary for both Eulerian and isopycnal frameworks. In addition, stationary solutions have been established only for the isopycnal-based kinetic equation. Therefore, we use the isopycnal-based formulation in Lvov et al. (2010) in our analysis. For clarity, we divide the review of theory into two parts.

1) FROM DYNAMIC EQUATIONS TO KINETIC EQUATION

We start from the primitive equations of motion in isopycnal coordinates (e.g., Cushman-Roisin and Beckers 2011; Lvov and Tabak 2001). The equations of mass conservation, horizontal momentum conservation (under the Boussinesq approximation) and hydrostatic balance can be written as

$$\frac{\partial}{\partial t}\frac{\partial z}{\partial \rho} + \nabla \cdot \left(\frac{\partial z}{\partial \rho}\mathbf{u}\right) = 0,$$

$$\frac{\partial \mathbf{u}}{\partial t} + f\mathbf{u}^\perp + \mathbf{u} \cdot \nabla \mathbf{u} + \frac{\nabla M}{\rho_0} = 0,$$

$$\frac{\partial M}{\partial \rho} - gz = 0, \qquad (11)$$

where ρ is the fluid density, ρ_0 is the reference fluid density, t is time, $\mathbf{u}(\mathbf{x}, \rho) \equiv (u, v)$ is the horizontal vector velocity at horizontal location $\mathbf{x} \equiv (x, y)$ and isopycnal coordinate ρ, $\mathbf{u}^\perp \equiv (-v, u)$, $z(\mathbf{x}, \rho)$ is the vertical depth (negative downward), $M(\mathbf{x}, \rho) \equiv P + \rho z$ is the Montgomery potential with P being the pressure, $\nabla \equiv (\partial/\partial x, \partial/\partial y)$, and g is the gravitational acceleration.

We note that the formulation in isopycnal coordinates results in a different definition of vertical wavenumber m from that in depth coordinates. For simplicity, we do not distinguish them symbolically. The usage of different m should be self-explanatory in different contexts in this paper.

Following Lvov et al. (2010), we seek a Hamiltonian formulation of (11) conserving the total energy. To this end, we decompose $\mathbf{u}$ as (e.g., Riley and Lelong 2000)

$$\mathbf{u} = \nabla \phi + \nabla^\perp \psi, \qquad (12)$$

with $\nabla^\perp \equiv (-\partial/\partial y, \partial/\partial x)$, and define a normalized differential layer thickness

$$\Pi = \rho_0 \frac{\partial z}{\partial \rho}. \qquad (13)$$

By assuming an initial profile of potential vorticity depending only on density, the variable ψ can be eliminated from the equations by considering the conservation of potential vorticity. The Hamiltonian system can then be formulated in terms of the variables ϕ and Π (see details in Lvov and Tabak 2004; Lvov et al. 2012),

$$\frac{\partial \Pi}{\partial t} = -\frac{\delta H}{\delta \phi}, \quad \frac{\partial \phi}{\partial t} = \frac{\delta H}{\delta \Pi}, \qquad (14)$$

with

$$H = \int d\mathbf{x}\, d\rho \left\{ -\frac{1}{2}\Pi \left|\nabla \phi + \nabla^\perp \Delta^{-1}(q_0\Pi - f)\right|^2 \right.$$
$$\left. + \frac{g}{2}\left|\int^\rho \rho' \frac{\Pi - \Pi_0}{\rho_0}\right|^2 \right\}, \qquad (15)$$

which is the sum of kinetic and potential energy, with $\Delta \equiv (\partial^2/\partial x^2, \partial^2/\partial y^2)$, $\Pi_0 = -g/N(\rho)^2$ as the reference layer thickness based on background buoyancy frequency, and $q_0 = f/\Pi_0(\rho)$ as the initial profile of potential vorticity.

We define the canonical variable $a_\mathbf{p}(t) \equiv a(\mathbf{p}, t)$ in Fourier space with $\mathbf{p} \equiv (\mathbf{k}, m)$ being the three-dimensional wavenumber:

$$\phi_\mathbf{p} = \frac{iN\sqrt{\omega_\mathbf{p}}}{\sqrt{2g}k}\left(a_\mathbf{p} - a_{-\mathbf{p}}^*\right),$$

$$\Pi_\mathbf{p} - \Pi_0 = -\frac{N\Pi_0 k}{\sqrt{2g\omega_\mathbf{p}}}\left(a_\mathbf{p} + a_{-\mathbf{p}}^*\right), \qquad (16)$$

where the frequency $\omega_\mathbf{p}$ satisfies the dispersion relation in isopycnal coordinates,

$$\omega_\mathbf{p} = \sqrt{f^2 + \frac{g^2}{\rho_0^2 N^2}\frac{k^2}{m^2}}. \qquad (17)$$

Equations (14) and (15) can then be transformed into the canonical form governing the evolution of the single variable $a_\mathbf{p}$. This is followed by introducing the spectral density of wave action as

$$n_\mathbf{p}\delta(\mathbf{p} - \mathbf{p}') = \left\langle a_\mathbf{p}^* a_{\mathbf{p}'}\right\rangle. \qquad (18)$$

The evolution equation of $n_\mathbf{p}$ can be derived by manipulation of the evolution equation of $a_\mathbf{p}$, which gives

$$\frac{\partial n_\mathbf{p}}{\partial t} = \mathscr{I}\int \left[V(\mathbf{p}, \mathbf{p}_1, \mathbf{p}_2)J(\mathbf{p}, \mathbf{p}_1, \mathbf{p}_2)\delta(\mathbf{p} - \mathbf{p}_1 - \mathbf{p}_2)\right.$$
$$\left. - 2V(\mathbf{p}_1, \mathbf{p}, \mathbf{p}_2)J(\mathbf{p}_1, \mathbf{p}, \mathbf{p}_2)\delta(\mathbf{p}_1 - \mathbf{p} - \mathbf{p}_2)\right] d\mathbf{p}_1\, d\mathbf{p}_2, \qquad (19)$$

where $\mathscr{I}$ denotes the imaginary part, and J is a triple correlation function with, e.g.,

$$J(\mathbf{p}, \mathbf{p}_1, \mathbf{p}_2)\delta(\mathbf{p} - \mathbf{p}_1 - \mathbf{p}_2) = \left\langle a_\mathbf{p}^* a_{\mathbf{p}_1} a_{\mathbf{p}_2}\right\rangle. \qquad (20)$$

The functions V are the interaction kernels that are derived in Lvov and Tabak (2004) and Lvov et al. (2010, 2012). However, the results presented in these papers are slightly different. We therefore rederive the functional form of V in appendix A, to ensure the validity of our numerical analysis of (19). We emphasize that the derivation up to (19) is exact (except for the mild assumption on the initial profile of potential vorticity), which describes the energy transfer to mode $\mathbf{p}$ due to all the resonant [i.e., satisfying

both (1) and (2)] and nonresonant [i.e., satisfying only (1)] triad interactions.

The following derivation for the kinetic equation is standard (e.g., Zakharov et al. 1992). We derive the evolution equation for J involving the quartet correlation function, which is approximated by a closure model under the assumption of quasi-Gaussian statistics. The solution of J is then substituted into (19). After assuming the dominance of resonant interactions, the final form of the kinetic equation reads

$$\frac{\partial n_{\mathbf{p}}}{\partial t} = \int \Big[4\pi |V(\mathbf{p},\mathbf{p}_1,\mathbf{p}_2)|^2 f_{p12}\delta(\mathbf{p}-\mathbf{p}_1-\mathbf{p}_2)\delta\left(\omega_{\mathbf{p}}-\omega_1-\omega_2\right) \\ - 8\pi |V(\mathbf{p}_1,\mathbf{p},\mathbf{p}_2)|^2 f_{1p2}\delta(\mathbf{p}_1-\mathbf{p}-\mathbf{p}_2)\delta\left(\omega_1-\omega_{\mathbf{p}}-\omega_2\right)\Big]\, d\mathbf{p}_1\, d\mathbf{p}_2, \tag{21}$$

with $f_{p12} \equiv n_{\mathbf{p}_1}n_{\mathbf{p}_2} - n_{\mathbf{p}}(n_{\mathbf{p}_1} + n_{\mathbf{p}_2})$, as an example. The integral on the right-hand side is usually termed as the "collision integral" (CL), describing the energy transfer (or action transfer) to mode $\mathbf{p}$ due to all the resonant triad interactions.

2) SOLUTION OF THE KINETIC EQUATION

We seek a stationary solution of the kinetic equation. Under the condition of horizontal isotropy, (21) (and the CL) can be simplified by integrating out the dependence on horizontal azimuth, yielding

$$\frac{\partial n_{\mathbf{p}}}{\partial t} = \int \frac{2}{k}\left(R_{p12} - 2R_{1p2}\right) dk_1\, dk_2\, dm_1\, dm_2, \tag{22}$$

where $R_{p12} = f_{p12}|V(\mathbf{p},\mathbf{p}_1,\mathbf{p}_2)|^2\delta(m-m_1-m_2)\delta(\omega_{\mathbf{p}} - \omega_1-\omega_2)kk_1k_2/S_{k12}$, with S_{k12} being the area of a triangle with sides k, k_1, and k_2.

The stationary power-law solution of (22) can be obtained by assuming a solution ansatz $n_{\mathbf{p}} \equiv n(\mathbf{k}, m) = k^{-a}m^{-b}$, and solving for a and b. Under scale-invariant considerations ($\omega \gg f$ so that f is neglected in the dispersion relation and kernel V), Lvov et al. (2010) find that the CL exhibits different properties of convergence/divergence at the infrared (IR, $k_{1,2} \to 0$) and ultraviolet (UV, $k_{1,2} \to \infty$) limits, depending on the values of a and b. These convergence and divergence behaviors physically indicate the dominance of local and nonlocal (or scale-separated) interactions. Three types of solutions can be found, lying in different regimes in terms of the convergence/divergence of the CL.

1) Convergent (C) solution: This belongs to the regime of CL converging at both the IR and UV limits, resulting in a solution of $a = 3.7$ and $b = 0$, which is close to the GM76 spectrum with $a = 4$ and $b = 0$.
2) Pelinovsky–Raevsky (PR) solution (Pelinovsky and Raevsky 1977): This belongs to the regime of CL diverging at both IR and UV limits, but with opposite-signed singularities that cancel each other. A family of PR solutions exist, e.g., $a = 3.5$, $b = 0.5$, or $a = 4.0$,

$b = 0$ where the latter is consistent with GM76 spectrum (Lvov et al. 2004).
3) Induced diffusion (ID) dominated solution: This belongs to the regime of CL converging at the UV limit and diverging at the IR limit. The divergence is however regularized by the inertial frequency as the cutoff frequency at the IR limit. By considering the ID nonlocal interactions [due to the previous studies (e.g., Müller et al. 1986)], solutions of this type lie on the ID lines $9 - 2a - 3b = 0$ or $b = 0$.

The regimes of CL and the three types of solutions are summarized in Fig. 2, along with a collection of field measurements (and our new result which will be discussed in section 4).

More analysis of these theoretical results is clearly required. In particular, it is not known what mechanism dominates the formation of the power-law spectra in the realistic ocean environment (even though most measurements seem to lie in the vicinity of the ID lines). A systematic way of using realistic data to investigate the mechanism in the framework of WTT is also highly desirable. In the following, we present such analysis using data from our new high-resolution ocean modeling.

3. High-resolution modeling of internal waves

In this section, we describe the numerical simulation that was used for high-resolution modeling of internal waves (HRMIW). Our focus is on a region in the Northeast Pacific (24°–32°N, 193°–199°E, see Fig. 3), which is characterized by an internal-tide beam emanating from the Hawaiian ridge that was previously investigated with intensive shipboard and moored observations (Alford et al. 2007). The lateral boundary conditions for the regional simulation are provided at hourly intervals by a hydrostatic, global-ocean configuration of the MITgcm, with nominal 1/48° horizontal grid spacing (~2 km in the 24°–32°N latitude band) and 90 vertical levels with 1-m vertical grid
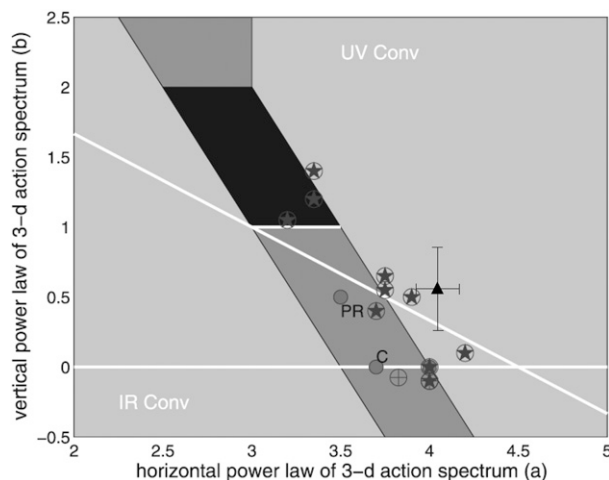
FIG. 2. Summary of regimes of the collision integral (CL), theoretical solutions, collection of previous measurements, and new result from high-resolution modeling of internal waves (HRMIW) on the map of (a, b). Filled circles: solutions of Pelinovsky–Raevsky (PR; $a = 3.5$, $b = 0.5$), convergent (C; $a = 3.7$, $b = 0$), and the GM76 ($a = 4$, $b = 0$) spectra. Two white lines: induced diffusion (ID)-dominated solutions. Circles with stars and crosshairs: previous field measurements at different locations. Triangle: new result from HRMIW in the region northwest of Hawaii, with uncertainty bars of 95% confidence level [computed assuming independent Gaussian distributions of the exponents in $E(\omega, m)$]. Light gray region: CL converges in either infrared (IR) or ultraviolet (UV) limit. Dark gray region: CL diverges at both IR and UV limits with opposite signs. Black region: CL diverges at both IR and UV limits with same signs. The figure is taken from Fig. 6 in Lvov et al. (2010), except for the new result from HRMIW.

spacing at the surface, gradually increasing to ~300 m near the 5000 m depth. A description of the 1/48° MITgcm simulation is available in Rocha et al. (2016) and Arbic et al. (2018). Of particular importance for the present study is that the global simulation is forced by both meteorological fields and tidal potential, that the spatial and temporal resolution is sufficient to resolve the low-mode internal tides, and that the full three-dimensional prognostic variables have been saved at hourly intervals. The 1/48° MITgcm simulation therefore provides realistic lateral boundary conditions for low-mode internal tides originating from throughout the Pacific Ocean.

In both the global and regional configurations, the ocean surface is forced with 6-hourly atmospheric fields from the 0.14° European Center for Medium-Range Weather Forecasts (ECMWF) Operational Model Analysis starting in 2011. Astronomical tides are applied using the full luni-solar potential. Horizontal eddy viscosity is parameterized using the scale-aware formulation of Fox-Kemper and Menemenlis (2008). There is no explicit horizontal tracer diffusivity. Vertical viscosity and diffusivity are parameterized according to the

K-profile parameterization (KPP) of Large et al. (1994). Tracer advection is based on the flux-limited, seventh-order, monotonicity-preserving advection scheme of Daru and Tenaud (2004). Bottom drag is quadratic with drag coefficient $C_d = 0.0021$, and side drag is free slip.

For the HRMIW regional configuration, the domain of integration has 2304 × 3744 horizontal grid cells, with ~250-m horizontal grid spacing and 264 vertical levels that have thicknesses ranging from 0.3 m near the surface to ~100 m near the 5000-m depth. The HRMIW configuration is integrated from 1 March 2012 to 15 June 2012 with an integration time step of 6 s. Model outputs are saved every 10 min. Lateral boundary conditions for the model's prognostic variables (potential temperature, salinity, velocity, and sea surface height) are prescribed from hourly snapshots of the global simulation, interpolated in time to the 6-s time step of the regional simulation. The lateral boundary conditions are prescribed exactly at every depth level, that is, without a sponge layer. We have verified, visually, that this does not cause artifacts near the open boundaries of the regional domain. Although some internal wave reflection does occur at the lateral boundaries, the reflected waves are of sufficiently high wavenumber that they, to a large extent, dissipate rapidly within the integration domain before reaching a neighboring boundary. These high-wavenumber reflected waves compensate, in part, for variability of the boundary conditions that is not represented in the global simulation (e.g., the subgrid waves).

The HRMIW regional simulation was carried out on the Niagara supercomputer (Ponce et al. 2019) operated by SciNet at the University of Toronto, using 60 000 CPU cores and requiring 1 PB of disk storage. The HRMIW simulation is described in detail in Nelson et al. (2020), including comparison with moored McLane profiler data (e.g., Alford et al. 2007; Zhao et al. 2010). The model–data comparisons show that the HRMIW simulation has very realistic power-law spectra relative to observations. In the present manuscript, we focus on the analysis of the generation mechanisms underlying oceanic internal gravity wave power-law spectra.

4. Results and analysis

a. Wave spectra and horizontal isotropy

We first examine the spectral slopes from the outputs of HRMIW. A typical frequency spectrum of kinetic energy $E^k(\omega)$, evaluated at 27.9°N, 195.3°E and 500-m depth, is plotted in Fig. 4. Remarkably, the spectrum shows a power-law range of over one decade in frequency
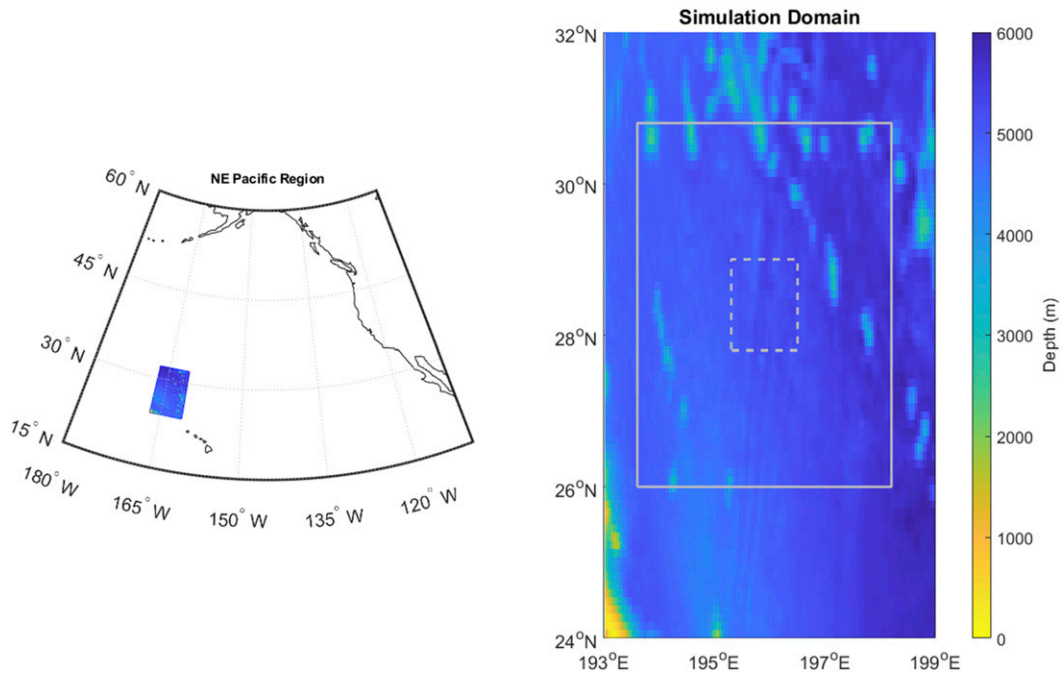
FIG. 3. (left) The northeast Pacific region showing a colored box at the location of the simulation domain. (right) A close-up of the simulation domain including the local bathymetry (color), and the regions H_1 (solid-line box) and H_2 (dash-line box) used in analysis in section 4.

(20–200 rad day^{-1}). The best linear fit of the power-law range [which provides the highest value of R^2 by varying the fitting range, as in Pan and Yue (2014)] gives a scaling of $\omega^{-2.2}$. Two peaks are observed at the inertial (f) and semidiurnal (M$_2$) frequencies, indicating that the near-inertial waves and internal tides are well captured by the regional model.

The spectral slopes are found to vary slightly depending on the location where the spectrum is evaluated. We quantify the range of variation by randomly sampling
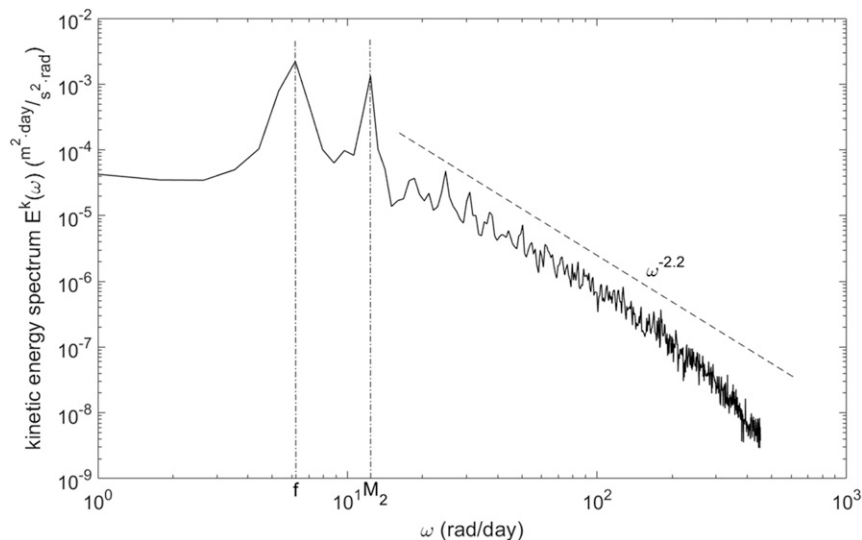

FIG. 4. Frequency spectrum of kinetic energy $E^k(\omega)$ at 195.3°E, 27.9°N and 500-m depth. The spectrum is evaluated as the average of 10 segments of 7.1 days in the time interval from 25 Apr to 24 May 2012. The inertial (f) and semidiurnal (M$_2$) frequencies are indicated with dash–dot lines.
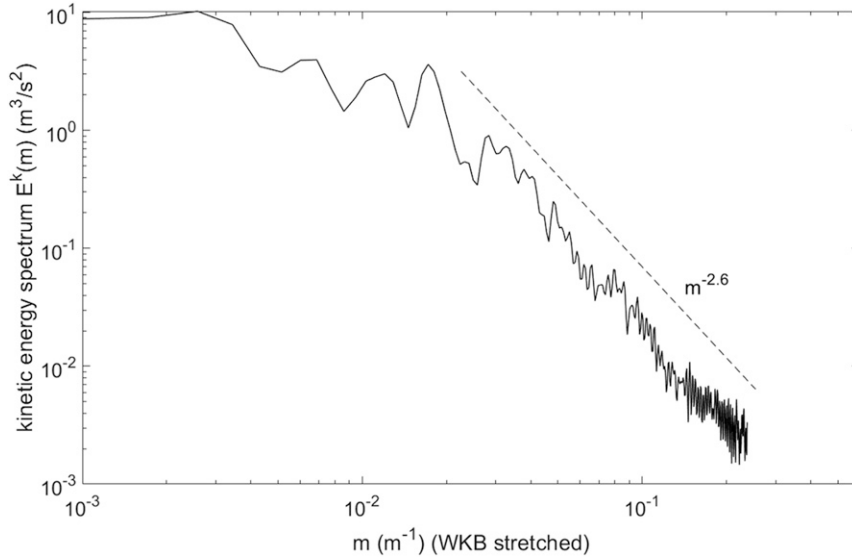
FIG. 5. Vertical wavenumber spectrum of kinetic energy $E^k(m)$ at 194.9°E, 27.4°N and depth range of $D_1 \equiv [172\,\text{m}, 2425\,\text{m}]$, averaged over 10 h on 27 Apr 2012. The WKB scaling and stretching are applied, and a Lomb–Scargle algorithm is used to handle the nonuniform grid.

and evaluating the spectrum at 50 points in a horizontal 512 km × 512 km domain H_1 (see Fig. 2) centered at (28.4°N, 195.9°E). This gives a scaling of $\omega^{-2.05\pm0.2}$, with the average slope very close to the GM76 spectrum (6).

We then evaluate the vertical-wavenumber spectrum $E^k(m)$ in the depth range of $D_1 \equiv [166\,\text{m}, 2247\,\text{m}]$, where the variation of buoyancy frequency is relatively mild. The WKB scaling and stretching (Leaman and Sanford 1975) are applied and a Lomb–Scargle algorithm (Thong et al. 2004) is used to handle the nonuniform grid. A typical spectrum is plotted in Fig. 5, with a best fit of the power-law range $m^{-2.6}$. The variation of the spectral slope in the H_1 domain is evaluated similarly as that for the frequency spectrum, with $m^{-2.58\pm0.4}$. The average spectral slope of m can be seen to deviate from the GM76 spectrum (7) by a value of 0.58.

The above analysis shows a spectral form of $E(\omega, m) \sim \omega^{-2.05}m^{-2.58}$ as the average of the model outputs [we note that the kinetic energy spectrum is sufficient to indicate the spectral slope of the total energy spectrum due to the polarization relations of internal waves (e.g., Polzin and Lvov 2011)]. Using (10), this energy spectrum corresponds to a wave action spectrum of $n(\mathbf{k}, m) \sim k^{-4.05}m^{-0.58}$. We have plotted this pair of spectral slopes on the map of (a, b) in Fig. 2, which is located in the vicinity of the ID line among a cluster of field measurements. More specifically, the numerical solution is much closer to the ID line than to the GM76 spectrum, with distances $O(0.2)$ and $O(0.6)$ on the (a, b) plane for the former and the latter.

We further check the horizontal isotropy of the internal wave field. Figure 6 plots the spectrum of $E(\mathbf{k})$ at 500-m depth. The condition of horizontal isotropy is well satisfied in this region, although the zoom-in inset for small wavenumbers shows some anisotropic flow at large scales, reflecting the internal tide beam propagating across the region. As measured in Alford et al. (2007), the internal tide in this region exhibits a clear feature of 80-km horizontal wavelength, which is consistent with the scale in the figure inset. Since the horizontal isotropy in the power-law range is a necessary condition to obtain the theoretical solutions (i.e., those in Fig. 2) of the kinetic equation, this analysis supports the interpretation of the spectral slopes in the framework of WTT.

We describe the horizontal distribution of energy using a one-dimensional spectrum $E(k) = \int_{-\pi}^{\pi} E^k(\mathbf{k})k\,d\theta$, where θ is the azimuth angle of $\mathbf{p}$ (or the direction of $\mathbf{k}$ in the horizontal plane), and $E^k(\mathbf{k})$ is the two-dimensional horizontal wavenumber spectrum of kinetic energy. This is plotted in Fig. 7, showing a power-law range with $k^{-2.2}$ over one decade. To obtain the corresponding GM76 spectral slope, we convert (3) into $E(k, \omega)$ [or $E(k, m)$] and integrate out ω (or m). This yields a dependence of $E(k) \sim k^{-2}$ for large k, which is close to the HRMIW result. Existing field measurements in other regions also report similar values, e.g., $E(k) \sim k^{-2.4}$ in the Internal Wave Experiment (IWEX) (Müller et al. 1978) and $E(k) \sim k^{-2}$ in the Midocean Acoustic Transmission Experiment (MATE) (Levine et al. 1986).
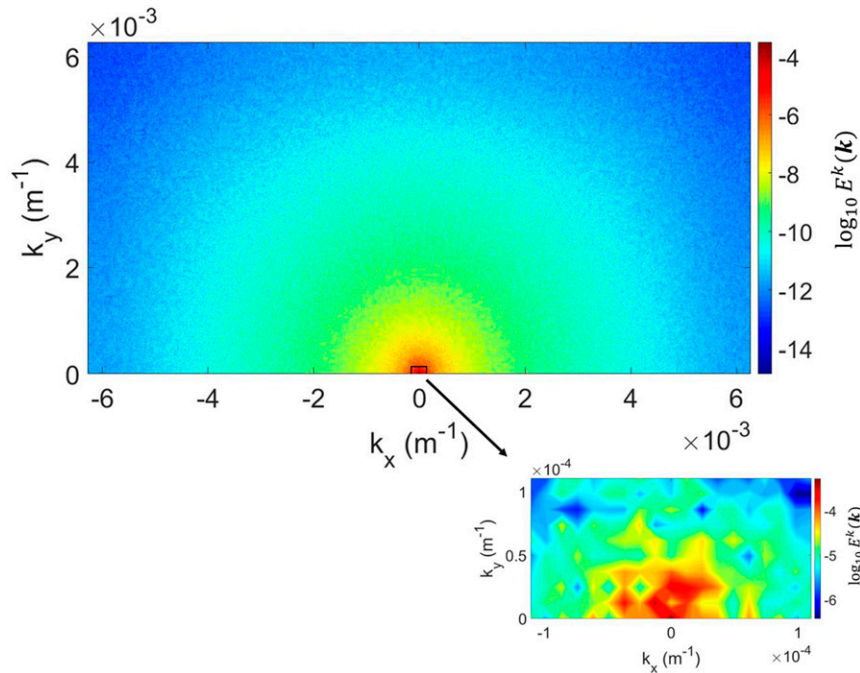
FIG. 6. Kinetic energy spectrum $E^k(\mathbf{k})$ ($m^4\,s^{-2}$), evaluated at 500-m depth, domain H_1, at one time instant on 29 Apr 2012. Only the part with $k_y > 0$ is plotted, as the other half satisfies first–third and second-fourth quadrant symmetry. Inset: the zoom-in view at large scales.

Before turning to the investigations of nonlinear interactions, we finally check the dispersion relation of the oscillations simulated in HRMIW. For this purpose, we plot the spectrum $E^k(k, \omega) = \int_{-\pi}^{\pi} E^k(\mathbf{k}, \omega)k\,d\theta$ in Fig. 8. In addition to the energy accumulation at forcing frequencies f and M_2, it is shown that the energy in the power-law range (marked in the figure) follows closely the linear curves of $\omega \sim k$. Five of these linear curves are indicated in the plot, which can be considered as the first five vertical modes of the internal waves. If a constant profile of N is assumed, these can be understood from the dispersion relation
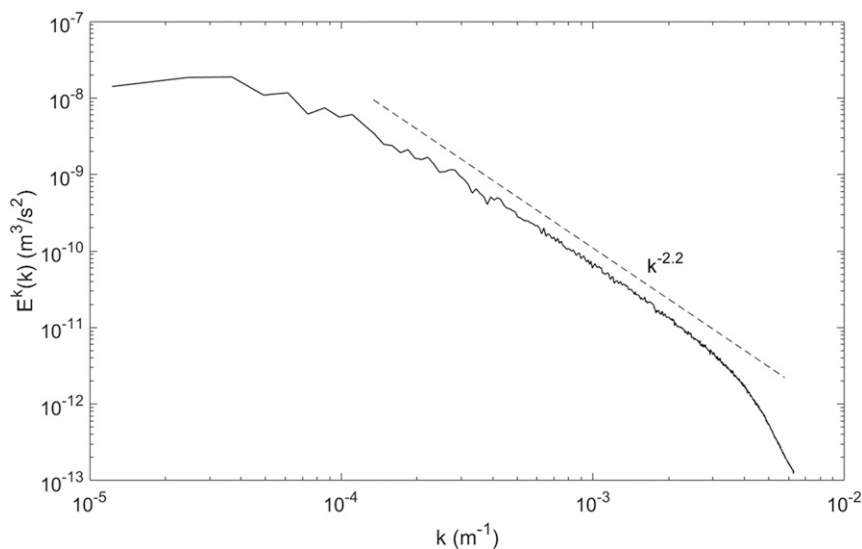

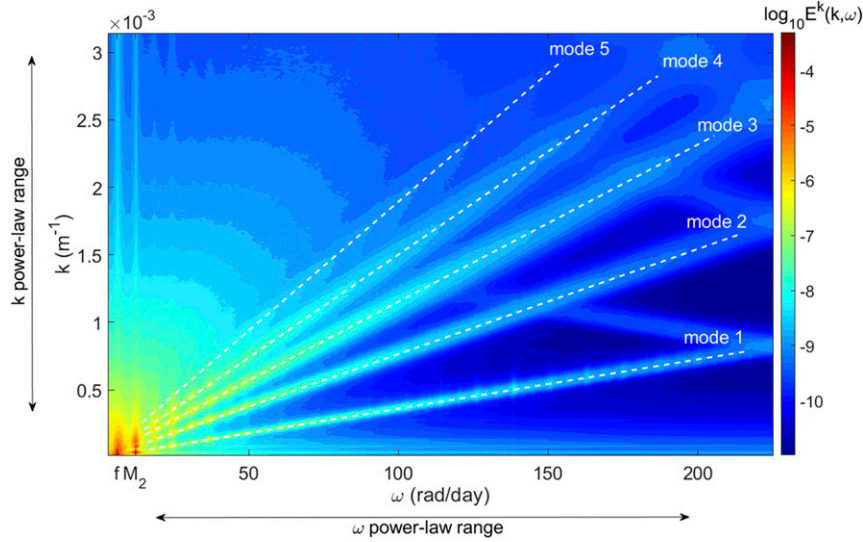FIG. 7. The one-dimensional spectrum $E^k(k)$ evaluated at 500 m, domain H_1, at one time instant on 29 Apr 2012.

FIG. 8. Kinetic energy spectrum $E^k(k, \omega)$ (m^3 day s^{-2} rad^{-1}) evaluated at 500 m, domain H_1, and during 3.5 days starting from 25 Apr 2012. The locations of most of the energy in the high-frequency, high-wavenumber portion of the spectrum are indicated by dashed lines, corresponding to the modes of internal waves. The power-law ranges in ω and k, as well as the inertial (f) and semidiurnal (M$_2$) frequencies are indicated in the figure.

(8) with $\omega \gg f$ for different vertical wavenumbers m. Alternatively, a more accurate representation can be obtained from the dispersion relation of vertical modes with varying N, where different curves correspond to different eigenspeeds of the modes (e.g., Müller et al. 2015). For the low-frequency low-wavenumber portion away from the power-law range, the energy for each mode is not distinguishable due to the convergence of all the dispersion relation curves (i.e., for small ω, the values of k for different modes are too close to be distinguished, and vice versa). Similar patterns have been found in Müller et al. (2015). Accounting for the inertial frequency f [see (8)], all the dispersion relation curves theoretically converge to (f, 0).

The satisfaction of the dispersion relation in the power-law range suggests that the formation of the spectrum is due to the existence of internal waves at these scales. An alternative check on this fact was conducted in Nelson et al. (2020) using internal wave consistency relations, demonstrating that the model is indeed resolving a portion of the internal wave spectrum.

b. Bicoherence analysis

In this section, we apply temporal and spatial bicoherence analysis to study the mode coupling in triad interactions. For a variable X, we define the temporal and spatial bicoherence as

$$B(\omega_1, \omega_2) = \frac{\left|\left\langle X^*(\omega_1 + \omega_2) X(\omega_1) X(\omega_2)\right\rangle^s\right|}{\left\langle |X(\omega_1 + \omega_2)||X(\omega_1)||X(\omega_2)|\right\rangle^s}, \quad (23)$$

$$B(\mathbf{p}_1, \mathbf{p}_2) = \frac{\left|\left\langle X^*(\mathbf{p}_1 + \mathbf{p}_2) X(\mathbf{p}_1) X(\mathbf{p}_1)\right\rangle^t\right|}{\left\langle |X(\mathbf{p}_1 + \mathbf{p}_2)||X(\mathbf{p}_1)||X(\mathbf{p}_2)|\right\rangle^t}, \quad (24)$$

where $\langle \ldots \rangle^s$ denotes the spatial average, $\langle \ldots \rangle^t$ the temporal average, and * the complex conjugate. As suggested in McComas and Briscoe (1980), any velocity component can be assigned to the variable X in (23) and (24), as long as it captures the spatial–temporal variations of internal waves. For our computation, we choose the zonal velocity for the variable X.

The temporal bicoherence (23) explores the normalized energy at ω_1, ω_2, and $\omega_1 + \omega_2$ that are phase coupled, which provides a measure of the strength of nonlinear interactions. The contour map of $B(\omega_1, \omega_1)$ is plotted in Fig. 9 [see captions for specific information on the evaluation of (23)]. For frequencies in the power-law range, most high values of B are concentrated in two straight lines with ω_1 or ω_2 close to the inertial frequency f. More specifically, for ω_1 (ω_2) in the power-law range, most couplings occur at $\omega_2 \approx f$ ($\omega_1 \approx f$). This highlights the importance of nonlocal interactions in forming the power-law spectrum, although the nature of the dominant nonlocal interactions in terms of energy transfer will be analyzed later in section 4c. In addition, for small values of ω_1 and ω_2 with $\omega_1 \approx \omega_2 \approx f$, there exists a region with
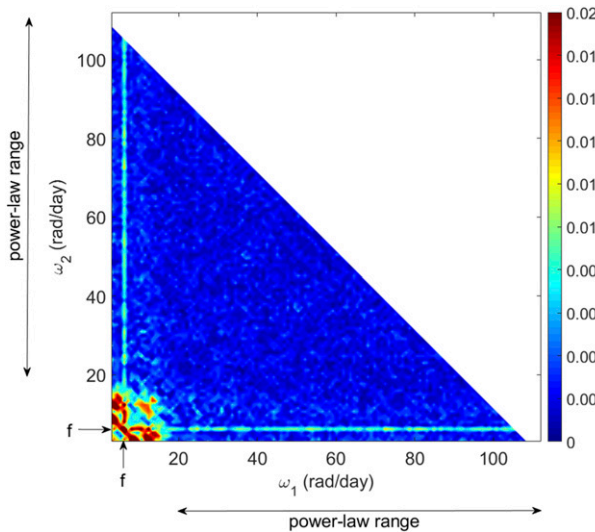
FIG. 9. Contour map of temporal bicoherence $B(\omega_1, \omega_2)$. For its evaluation using (23), $X(\omega)$ is calculated from 7-day time series of zonal velocity with 40-min intervals, starting from 25 Apr. The spatial average is performed in the domain $H_1 \times D_1$. The frequency power-law range and inertial frequency are indicated in the figure.

strong coupling. These interactions are due to the PSI, which is strong in the present region with $2f \approx M_2$.

The statistical significance of $B(\omega_1, \omega_2)$, with respect to the criterion set forth in McComas and Briscoe (1980), must be considered with caution. Based on values of $B(\omega_1, \omega_2)$ computed from for a GM76 spectrum, McComas and Briscoe (1980) assert that, to attain a 95% confidence level on $B(\omega_1, \omega_2)$, one needs data to cover at least $\nu = O(1000)$ fundamental wave periods [using the statistical relation $\nu = 4/B(\omega_1, \omega_2)^2$ (Haubrich 1965)]. For field measurements where data are taken at a single location, this requires about 3 years of data which is well beyond what is normally done

in field experiments. However, in our high-resolution simulation, data are taken from both space and time, which significantly reduces the required time interval. In particular, to compute $B(\omega_1, \omega_2)$ in Fig. 9, 128^3 time series are taken, with each of them containing 7 days of data. This is $O(10\,000)$ times of data required by the criterion for the results to be statistically significant. Indeed, we have tested the results averaged with varying amounts of data, which reveal consistently the same nonlocal interaction physics with the clear peak maintained at the inertial frequency.

In principle, the large value of ν is caused by the small values of $B(\omega_1, \omega_2)$ due to the relation $\nu = 4/B(\omega_1, \omega_2)^2$. As shown in Fig. 9, $B(\omega_1, \omega_2) \sim O(0.01)$ for its peak values, which are consistent with the theoretical estimation by McComas and Briscoe (1980). The small $B(\omega_1, \omega_2)$ is physically related to the dispersion relation (8) of internal waves, which implies that one value of frequency correspond to many modes (whose wavenumbers lie on a conical surface in the three-dimensional space). With the numerator of (23) selecting only modes involving resonances, and normalized by total energy of all modes lying on the conical surfaces, the resulting values of $B(\omega_1, \omega_2)$ are small (see appendix B for a more detailed analysis). A different consideration arises from the usage of the spatial bicoherence (24). Since each vector wavenumber corresponds to a single frequency (or single wave mode), the normalized value $B(\mathbf{p}_1, \mathbf{p}_2)$ is $O(1)$ (which is confirmed in our analysis), subject to a much smaller ν [although more data are required for evaluation of $X(\mathbf{p})$ than for that of $X(\omega)$].

We next evaluate (24), which explores the coupling of three wavenumber modes $\mathbf{p}_1$, $\mathbf{p}_2$, and $\mathbf{p}_1 + \mathbf{p}_2$. For easier visualization, we fix the value of $\mathbf{p}_1$ and examine B as a function of $\mathbf{p}_2$ only, i.e., $B(\mathbf{p}_2; \mathbf{p}_1)$. To measure the distribution of $\mathbf{p}_2$ for the strong-coupling triads, we further define a density function

$$\gamma(\Omega, \chi; \mathbf{p}_1) = \frac{\#\left\{\mathbf{p}_2 \middle| B(\mathbf{p}_2; \mathbf{p}_1) > 0.1, \Omega - \frac{\Delta\Omega}{2} < \omega_2 < \Omega + \frac{\Delta\Omega}{2}, \chi - \frac{\Delta\chi}{2} < |m_2| < \chi + \frac{\Delta\chi}{2}\right\}}{\chi\kappa\Delta\Omega\Delta\chi}, \tag{25}$$

where (Ω, χ) is a point on the 2D plane of $(\omega_2, |m_2|)$, $\Delta\Omega$ and $\Delta\chi$ are small intervals around Ω and χ, $\#$ denotes the number of elements in the set, κ is the horizontal wavenumber calculated from (Ω, χ) by the dispersion relation (8). The denominator of (25) provides a measure of the volume in 3D $(\mathbf{k}, m)$ space corresponding to $(\Omega \pm \Delta\Omega/2, \chi \pm \Delta\chi/2)$. Therefore, given $\mathbf{p}_1$, $\gamma(\Omega, \chi; \mathbf{p}_1)$ calculates the density of strong-coupling triads (with $B(\mathbf{p}_2; \mathbf{p}_1) > 0.1$) in $(\mathbf{k}, m)$ space in the vicinity of $\omega_2 = \Omega$ (or $k_2 = \kappa$) and $|m_2| = \chi$. We note that the value of

$\gamma(\Omega, \chi; \mathbf{p}_1)$ varies with different discretizations and sizes of the physical (or Fourier) domain. For our calculation, we use a $128 \times 128 \times 128$ discretization of the domain $H_1 \times D_1$, corresponding to the fundamental horizontal and vertical wavenumbers $\mathscr{K}^{11} = 1.2 \times 10^{-5}\,\mathrm{m}^{-1}$ and $\mathscr{M}^{11} = 3 \times 10^{-3}\,\mathrm{m}^{-1}$ (where the superscripts represent the indices of H and D).

We select two vectors of $\mathbf{p}_1^V$ and $\mathbf{p}_1^H$ with more vertical and more horizontal orientations, corresponding to lower and higher frequencies in the range of the power-law
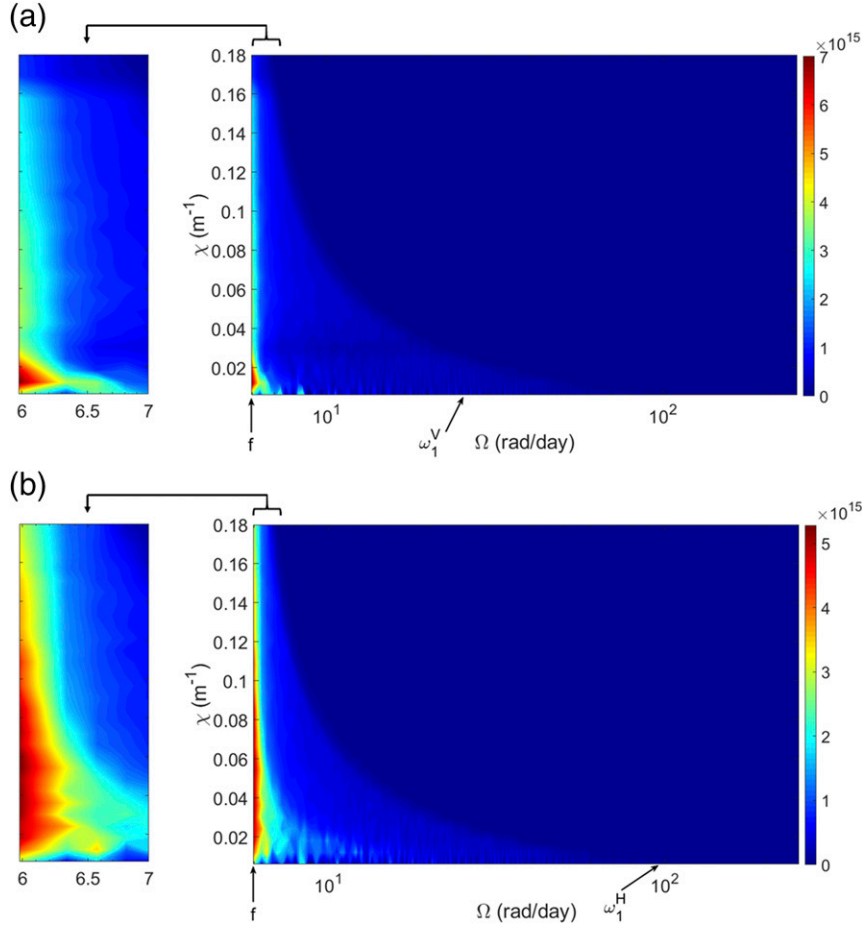
FIG. 10. Function $\gamma(\Omega, \chi; \mathbf{p}_1)$ evaluated in domain $H_1 \times D_1$ with a $128 \times 128 \times 128$ discretization, corresponding to the fundamental horizontal and vertical wavenumbers $\mathscr{K}^{11} = 1.2 \times 10^{-5} \, \mathrm{m}^{-1}$ and $\mathscr{M}^{11} = 3 \times 10^{-3} \, \mathrm{m}^{-1}$. The zoom-in views of the high intensity regions are shown on the left. For the calculation in (25), we use $\Delta\chi = 2\mathscr{M}^{11}$ and $\Delta\Omega = 0.04f$. The time average in calculating $B(\mathbf{p}_2; \mathbf{p}_1)$ is taken in a 7-day interval starting from 25 Apr 2012. The values of $\gamma(f, \chi; \mathbf{p}_1)$ are evaluated with forward difference instead of central difference in (25). (a) $\gamma(\Omega, \chi; \mathbf{p}_1^V)$ with $\mathbf{p}_1^V = (60\mathscr{K}^{11}, 60\mathscr{K}^{11}, 10\mathscr{M}^{11}) = (7.2 \times 10^{-4}, 7.2 \times 10^{-4}, 0.03) \, \mathrm{m}^{-1}$ and $\omega_1^V = 24.2 \, \mathrm{rad\,day}^{-1}$; (b) $\gamma(\Omega, \chi; \mathbf{p}_1^H)$ with $\mathbf{p}_1^H = (48\mathscr{K}^{11}, 48\mathscr{K}^{11}, 2\mathscr{M}^{11}) = (5.8 \times 10^{-4}, 5.8 \times 10^{-4}, 0.006) \, \mathrm{m}^{-1}$ and $\omega_1^H = 94 \, \mathrm{rad\,day}^{-1}$. The inertial frequency f and values of ω_1 are indicated in both (a) and (b).

frequency spectrum. Specifically, $\mathbf{p}_1^V = (60\mathscr{K}^{11}, 60\mathscr{K}^{11}, 10\mathscr{M}^{11})$ with $\omega_1^V = 24.2 \, \mathrm{rad\,day}^{-1}$, $\mathbf{p}_1^H = (48\mathscr{K}^{11}, 48\mathscr{K}^{11}, 2\mathscr{M}^{11})$ with $\omega_1^H = 94 \, \mathrm{rad\,day}^{-1}$. The functions $\gamma(\Omega, \chi; \mathbf{p}_1^V)$ and $\gamma(\Omega, \chi; \mathbf{p}_1^H)$ are plotted in Fig. 10. We see that both $\gamma(\Omega, \chi; \mathbf{p}_1^V)$ and $\gamma(\Omega, \chi; \mathbf{p}_1^H)$ achieve high values for small Ω, indicating a higher density of strong-coupling triads for $\omega_2 \to f$, which provides another demonstration of the importance of nonlocal interactions in forming the power-law spectrum. Among the strong-coupling triads with $\omega_2 \to f$, the value of m_2 spreads significantly along the vertical axis. This large range of m_2 for the strong-coupling triads shows that these nonlinear interactions can be ES, ID, and many others that are not defined by the three types

of traditional nonlocal interactions (Fig. 1). However, it should be kept in mind that the occurrence of nonlinear interactions does not imply significant energy transfer. The detailed analysis of the triads dominating the energy transfer will be provided in section 4c.

c. Mechanism in the framework of WTT

Although both the temporal and spatial bicoherence analyses emphasize the importance of nonlocal interactions, they provide no information on the quantitative energy transfer, which governs the CL and spectral slopes in WTT. Our goal in this section is to examine the CL and the associated energy transfer (or action transfer) using the

HRMIW outputs and connect the result with the spectral slopes evaluated in section 4a.

Instead of directly evaluating the CL in (21) (or 22), we consider both the resonant and nonresonant triad interactions which contribute to the energy transfer to a mode **p**, as the nonresonant interactions also play an important role in the realistic ocean environment. This requires the evaluation of (19) using the model outputs. To this end, we reformulate (19) in discrete form (e.g., Nazarenko 2011)

$$\frac{\partial n_{\mathbf{p}}}{\partial t} = \mathscr{T} \sum_{\mathbf{p}=\mathbf{p}_1+\mathbf{p}_2} V(\mathbf{p},\mathbf{p}_1,\mathbf{p}_2)\left\langle a_{\mathbf{p}}^* a_{\mathbf{p}_1} a_{\mathbf{p}_2}\right\rangle$$
$$-2\mathscr{T} \sum_{\mathbf{p}_1=\mathbf{p}+\mathbf{p}_2} V(\mathbf{p}_1,\mathbf{p},\mathbf{p}_2)\left\langle a_{\mathbf{p}_1}^* a_{\mathbf{p}} a_{\mathbf{p}_2}\right\rangle, \quad (26)$$

resulting from a Fourier series definition of $a_{\mathbf{p}}$ and $n_{\mathbf{p}} = \langle a_{\mathbf{p}} a_{\mathbf{p}}^*\rangle$. In this section, we focus on the analysis of action transfer, and the energy transfer can be directly calculated from (26) by using $\partial n_{\mathbf{p}}/\partial t = (1/\omega_{\mathbf{p}})\partial E_{\mathbf{p}}/\partial t$ with $E_{\mathbf{p}}$ being the spectral energy density at mode **p**.

For the evaluation of (26), we focus on the domain $H_2 \times D_2$, where H_2 (see Fig. 2) is a 128 km × 128 km horizontal plane, and $D_2 = [1026, 1034]$ kg m^{-3} (vertically about [170 m, 1460 m]), with a 128 × 128 × 128 discretization. The corresponding fundamental horizontal and vertical wavenumbers are $\mathscr{K}^{22} = 4.9 \times 10^{-5}$ m^{-1} and $\mathscr{M}^{22} = 0.785$ m^3 kg^{-1}. Estimated by the dispersion relation (17), the discretized wave modes cover all the frequencies in the power-law range resolved in Fig. 4. The time averages for the triple moments are calculated with two days of output data with an interval of 10 min, which allows the frequency of almost all the discretized wave modes to be resolved (up to the order of buoyancy frequency). The model outputs in $H_2 \times D_2$ are interpolated to the isopycnal coordinates. The variable $a_{\mathbf{p}}$ is evaluated from (16) using $\Pi_{\mathbf{p}}$ and $\psi_{\mathbf{p}}$, where the former is computed from (13), and the latter is computed from (12) by subtracting the rotational component from the velocity field. The interaction coefficients V are calculated as summarized in appendix A.

To better interpret the results, we rewrite (26) as

$$\frac{\partial n_{\mathbf{p}}}{\partial t} = \sum_{\mathbf{p}_2} T(\mathbf{p}_2;\mathbf{p}), \quad (27)$$

where

$$T(\mathbf{p}_2;\mathbf{p}) = \mathscr{T}\left\{ V(\mathbf{p},\mathbf{p}-\mathbf{p}_2,\mathbf{p}_2)\left\langle a_{\mathbf{p}}^* a_{\mathbf{p}-\mathbf{p}_2} a_{\mathbf{p}_2}\right\rangle \right.$$
$$\left. - 2V(\mathbf{p}+\mathbf{p}_2,\mathbf{p},\mathbf{p}_2)\left\langle a_{\mathbf{p}+\mathbf{p}_2}^* a_{\mathbf{p}} a_{\mathbf{p}_2}\right\rangle \right\}, \quad (28)$$

calculates the transfer of wave action to mode **p** by triads involving another mode $\mathbf{p}_2$. We plot in Fig. 11a $T(\mathbf{p}_2;\mathbf{p})$ against k_2 for all $\mathbf{p}_2$ and a representative wavenumber
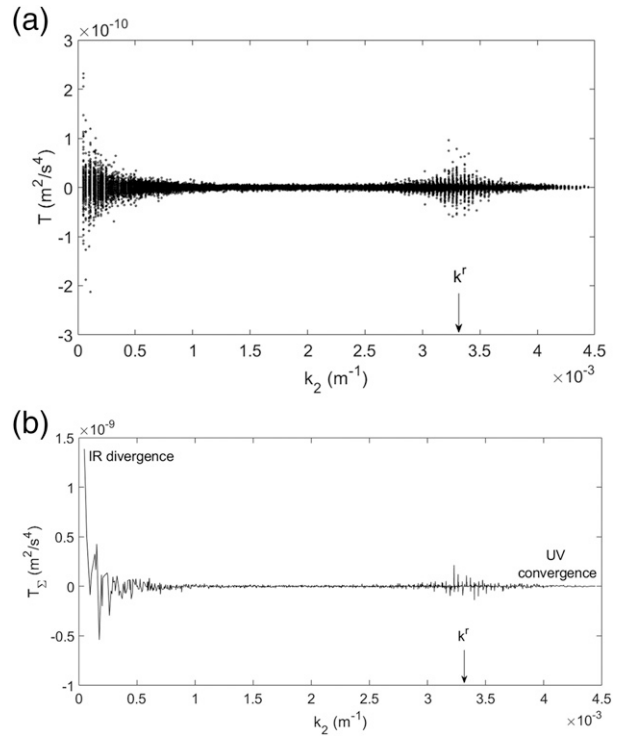

FIG. 11. (a) $T(\mathbf{p}_2;\mathbf{p}^r)$ against k_2 for all $\mathbf{p}_2$ and a representative vector $\mathbf{p}^r$ in the power-law range with $\mathbf{p}^r = (48\mathscr{K}^{22}, 48\mathscr{K}^{22}, 16\mathscr{M}^{22}) = (0.0024\,\text{m}^{-1}, 0.0024\,\text{m}^{-1}, 12.5\,\text{m}^3\,\text{kg}^{-1})$ and $\omega^r = 28.4$ rad day^{-1} from (17). (b) $T_{\Sigma}(k_2;\mathbf{p}^r)$ indicating IR divergence and UV convergence. The position of k^r calculated from $\mathbf{p}^r$ is indicated in both panels.

vector $\mathbf{p} = \mathbf{p}^r$ in the power-law range, with $\mathbf{p}^r = (48\mathscr{K}^{22}, 48\mathscr{K}^{22}, 16\mathscr{M}^{22})$ and $\omega^r = 28.4$ rad day^{-1}. It is shown in Fig. 11a that all the high values of T occur in the vicinity of $k_2 \approx 0$ and $k_2 \approx k^r$. While the former indicates the dominance of nonlocal interactions in energy transfer, the latter results from the symmetry of the triad $\mathbf{p} = \mathbf{p}_1 + \mathbf{p}_2$ that will be discussed shortly.

To make a direct connection from $T(\mathbf{p}_2;\mathbf{p})$ to the CL, we define $T_{\Sigma}(k_2;\mathbf{p}) = \sum_{m_2,\theta_2} T(\mathbf{p}_2;\mathbf{p})$, which calculates the action transfer to mode **p** via all triads having a mode with horizontal wavenumber k_2. Therefore, it evaluates the CL in the vicinity of k_2 by further including the contribution of nonresonant triads. The function $T_{\Sigma}(k_2;\mathbf{p}^r)$ is plotted in Fig. 11b, which exhibits high values for $k_2 \to 0$ and approaches zero for large k_2. Referring to WTT, this means that the CL diverges (and gets regularized) at the IR limit and converges at UV limit.

We further explore the specific triad interactions leading to the IR divergence behavior. For this purpose, we decompose $T(\mathbf{p}_2;\mathbf{p}) = T_1(\mathbf{p}_2;\mathbf{p}) + 2T_2(\mathbf{p}_2;\mathbf{p})$, where

$$T_1(\mathbf{p}_2;\mathbf{p}) = \mathscr{T} V(\mathbf{p},\mathbf{p}-\mathbf{p}_2,\mathbf{p}_2)\left\langle a_{\mathbf{p}}^* a_{\mathbf{p}-\mathbf{p}_2} a_{\mathbf{p}_2}\right\rangle, \quad (29)$$

and

$$T_2(\mathbf{p}_2; \mathbf{p}) = -\mathscr{T} V(\mathbf{p} + \mathbf{p}_2, \mathbf{p}, \mathbf{p}_2)\langle a^*_{\mathbf{p}+\mathbf{p}_2} a_{\mathbf{p}} a_{\mathbf{p}_2}\rangle, \qquad (30)$$

correspond to the action transfers due to, respectively, the triads $\mathbf{p} = \mathbf{p}_1 + \mathbf{p}_2$ and $\mathbf{p}_1 = \mathbf{p} + \mathbf{p}_2$. The functions $T_1(\mathbf{p}_2; \mathbf{p}^r)$ and $T_2(\mathbf{p}_2; \mathbf{p}^r)$ are plotted in Fig. 12 against k_2. It is shown that the action transfer via T_1 achieves high values of complete symmetry near $k_2 \approx 0$ and $k_2 \approx k^r$, due to the symmetry of $\mathbf{p}_1$ and $\mathbf{p}_2$ in the triad $\mathbf{p} = \mathbf{p}_1 + \mathbf{p}_2$. This also explains the high values near $k_2 \approx k^r$ observed in Fig. 11. The action transfer via T_2, on the other hand, has its high values mainly located near $k_2 \approx 0$ without the symmetry. Therefore, the IR divergence results from the combined contributions of both triads T_1 and T_2.

The above analysis has illustrated the nonlocal interactions as the main mechanism in the formation of the power-law spectra of internal waves. The nature of these interactions is, however, yet to be identified. To answer this question, we consider the triads $T_2(\mathbf{p}_2; \mathbf{p}^r)$ (without loss of generality) and focus on the set $S(\mathbf{p}^r) = \{\mathbf{p}_2 || T_2(\mathbf{p}_2; \mathbf{p}^r)| > 0.4 \max[|T_2(\mathbf{p}_2; \mathbf{p}^r)|]\}$, representing those $\mathbf{p}_2$ resulting in significant energy transfer. Since such $\mathbf{p}_2$ values correspond to low-frequency modes, we can describe ID as $|m_2/m^r| \ll 1$, $\omega_2/\omega^r \ll 1$, PSI as $|m_2/m^r| \gg 1$, $\omega_2/\omega^r \approx 1/2$, and ES as $|m_2/m^r| \approx 2$, $\omega_2/\omega^r \ll 1$ (see Fig. 1). We define four representative modes $\mathbf{p}^r$ in the power-law range, to ensure all mechanisms can be captured in our finite-resolution discrete Fourier space (for at least one of these $\mathbf{p}^r$s). These representative modes are denoted by $\mathbf{p}^r_{H(L),H(L)}$ (see Fig. 13 caption for exact vector values), with the first subscript meaning high wavenumber (low wavenumber) and second subscript meaning high frequency (low frequency). Considering our discrete resolution in $\mathbf{p}$, ID can be resolved in $S(\mathbf{p}^r_{L,L})$ and $S(\mathbf{p}^r_{L,H})$, PSI in $S(\mathbf{p}^r_{L,L})$ and $S(\mathbf{p}^r_{L,H})$, and ES in all $S(\mathbf{p}^r)$.

The vectors $\mathbf{p}_2$ in the set $S(\mathbf{p}^r)$ are plotted in Figs. 13a–d for $S(\mathbf{p}^r_{H,L})$, $S(\mathbf{p}^r_{H,H})$, $S(\mathbf{p}^r_{L,L})$, and $S(\mathbf{p}^r_{L,H})$, respectively. Specifically, each vector $\mathbf{p}_2$ is shown as a dot in the plane of $(m_2/m^r, \omega_2/\omega^r)$, with color denoting $|T_2(\mathbf{p}_2; \mathbf{p}^r)|/\max[|T_2(\mathbf{p}_2; \mathbf{p}^r)|]$, i.e., strength of energy transfer. In Figs. 13a and 13b, we indeed see that most of the dominant interactions are located in the ID regime with $|m_2/m^r| \ll 1$ and $\omega_2/\omega^r \ll 1$. In Figs. 13c and 13d, PSI is absent, since all the interactions are confined in the regime of $|m_2/m^r| < 1$ (ID is not resolvable for $\mathbf{p}^r_{L,L}$ and $\mathbf{p}^r_{L,H}$). ES is absent in all subfigures, as no interaction has the feature of $|m_2/m^r| \approx 2$.

We further analyze the deviations from ID in Figs. 13a and 13b, i.e., those interactions with relatively larger $|m_2/m^r|$ and/or ω_2/ω^r. In particular, we are interested in whether nonresonant (or near-resonant) interactions
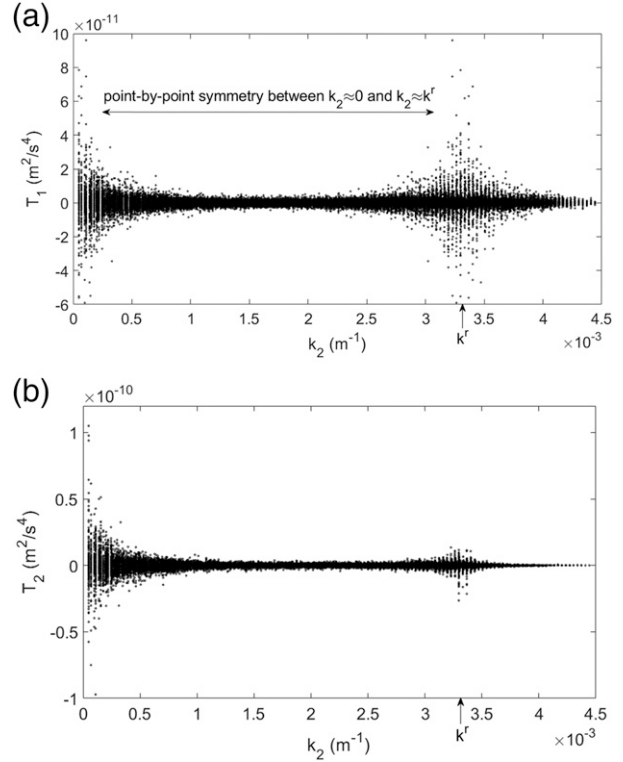

FIG. 12. (a) $T_1(\mathbf{p}_2; \mathbf{p}^r)$ and (b) $T_2(\mathbf{p}_2; \mathbf{p}^r)$ plotted against k_2. The position of k^r calculated from $\mathbf{p}^r$ is indicated in both panels.

result in these deviations. For this test, we define the mismatch of the T_2 triad frequencies

$$\Delta\omega = \omega_1 - \omega^r - \omega_2, \qquad (31)$$

and a variable measuring the deviation from ID

$$d_{\mathrm{ID}} = \sqrt{(m_2/m^r)^2 + (\omega_2/\omega^r)^2}, \qquad (32)$$

which achieves higher values for larger deviations. We plot the function $d_{\mathrm{ID}}(\Delta\omega/f)$ in Fig. 14, with Figs. 14 and 14b corresponding to the interactions in Figs. 13a and 13b. For both subfigures, we see that d_{ID} achieves minimum value for $\Delta\omega \to 0$, and d_{ID} increase as $\Delta\omega$ moves away from 0. This indicates that the deviation from the ID mechanism is indeed caused by the near-resonant interactions, enabled by the nonlinear broadening (e.g., Lvov et al. 2012). Therefore, the main mechanism for transferring energy in the power-law range of the spectrum is identified as ID with a finite broadening in its vicinity. This is consistent with the spectral slopes resolved in the model (section 4a), which is close to the ID-dominated solutions in Fig. 2.

Finally, we remark that this analysis does not exclude the existence of PSI and ES. It simply shows that they are not dominant in transferring energy in the power-law
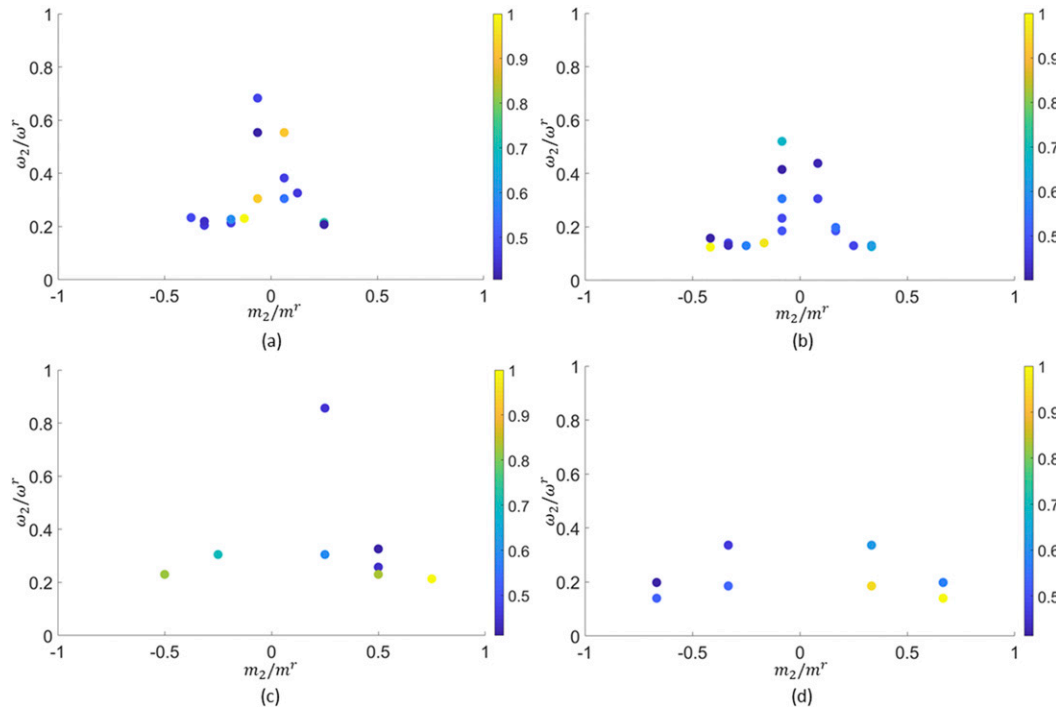
FIG. 13. Vectors of wavenumber $\mathbf{p}_2$ in the set $S(\mathbf{p}^r) = \{\mathbf{p}_2 \big| |T_2(\mathbf{p}_2; \mathbf{p}^r)| > 0.4\max[|T_2(\mathbf{p}_2; \mathbf{p}^r)|]\}$, plotted as dots in the plane of $(m_2/m^r, \omega_2/\omega^r)$, with color denoting the values of $|T_2(\mathbf{p}_2; \mathbf{p}^r)|/\max[|T_2(\mathbf{p}_2; \mathbf{p}^r)|]|$. Shown are (a) $\mathbf{p}_{H,L}^r = (48\mathcal{K}^{22}, 48\mathcal{K}^{22}, 16\mathcal{M}^{22}) = (0.0024\,\text{m}^{-1}, 0.0024\,\text{m}^{-1}, 12.5\,\text{m}^3\,\text{kg}^{-1})$, with $\omega^r = 28.4\,\text{rad day}^{-1}$; (b) $\mathbf{p}_{H,H}^r = (60\mathcal{K}^{22}, 60\mathcal{K}^{22}, 12\mathcal{M}^{22}) = (0.003\,\text{m}^{-1}, 0.003\,\text{m}^{-1}, 9.4\,\text{m}^3\,\text{kg}^{-1})$, with $\omega^r = 46.8\,\text{rad day}^{-1}$; (c) $\mathbf{p}_{L,L}^r = (12\mathcal{K}^{22}12\mathcal{K}^{22}, 4\mathcal{M}^{22}) = (0.0006\,\text{m}^{-1}, 0.0006\,\text{m}^{-1}, 3.1\,\text{m}^3\,\text{kg}^{-1})$ with $\omega^r = 28.4\,\text{rad day}^{-1}$; and (d) $\mathbf{p}_{L,H}^r = (15\mathcal{K}^{22}, 15\mathcal{K}^{22}, 3\mathcal{M}^{22}) = (0.00075\,\text{m}^{-1}, 0.00075\,\text{m}^{-1}, 2.4\,\text{m}^3\,\text{kg}^{-1})$ with $\omega^r = 46.8\,\text{rad day}^{-1}$.

range, although they can be dominant in other portions of the spectrum, e.g., PSI in tidal damping in the low-frequency range. Also, there might exist other mechanisms that contribute to forming the power-law spectra in the real ocean, e.g., convergent or PR solutions discussed in section 2, and in driving the energy cascade, e.g., wave–eddy interactions (Barkan et al. 2017). A comprehensive understanding of these mechanisms in the realistic ocean environment will require further study.

5. Discussion and conclusions

We have studied the mechanisms involved in the formation of the power-law spectra of internal waves by analyzing the numerical data from a high-resolution ocean model. The model captures the power-law spectrum in broad ranges of frequency and wavenumber, with satisfaction of horizontal isotropy and $E(\omega, m) \sim \omega^{-2.05\pm0.2}m^{-2.58\pm0.4}$. This corresponds to a wave action spectrum lying in the vicinity of induced diffusion dominated solutions according to wave turbulence theory, resulting mathematically from the collision integral diverging in the infrared limit. To study the nonlinear triad interactions from the numerical data, we first applied bicoherence

analysis, which suggests the importance of nonlocal (i.e., scale separated) interactions. We then cast the model outputs into the framework of wave turbulence theory and investigated the collision integral with additional contributions from the nonresonant interactions that play an important role in the context of the realistic ocean. The numerical results confirm the dominance of the energy transfer by the interaction with the low-frequency modes. The strong interactions are further identified as involving induced diffusion (ID) and the near-resonant interactions in its neighborhood enabled by nonlinear broadening. These findings on the nature of nonlinear interactions are consistent with the spectral slopes resolved by the model, which are close to the slopes in the ID-dominated stationary solution in the framework of wave turbulence theory.

Further analysis using the output from high-resolution ocean models are warranted, which may shed light on many outstanding problems in physical oceanography. We envision two directions in our future work. First, we will seek to understand whether the high-resolution output can be used to establish the connection between the spectral form of internal waves and the depth dependence of the (background) diapycnal diffusivity in the ocean. In particular, we are interested in whether the finescale parameterization
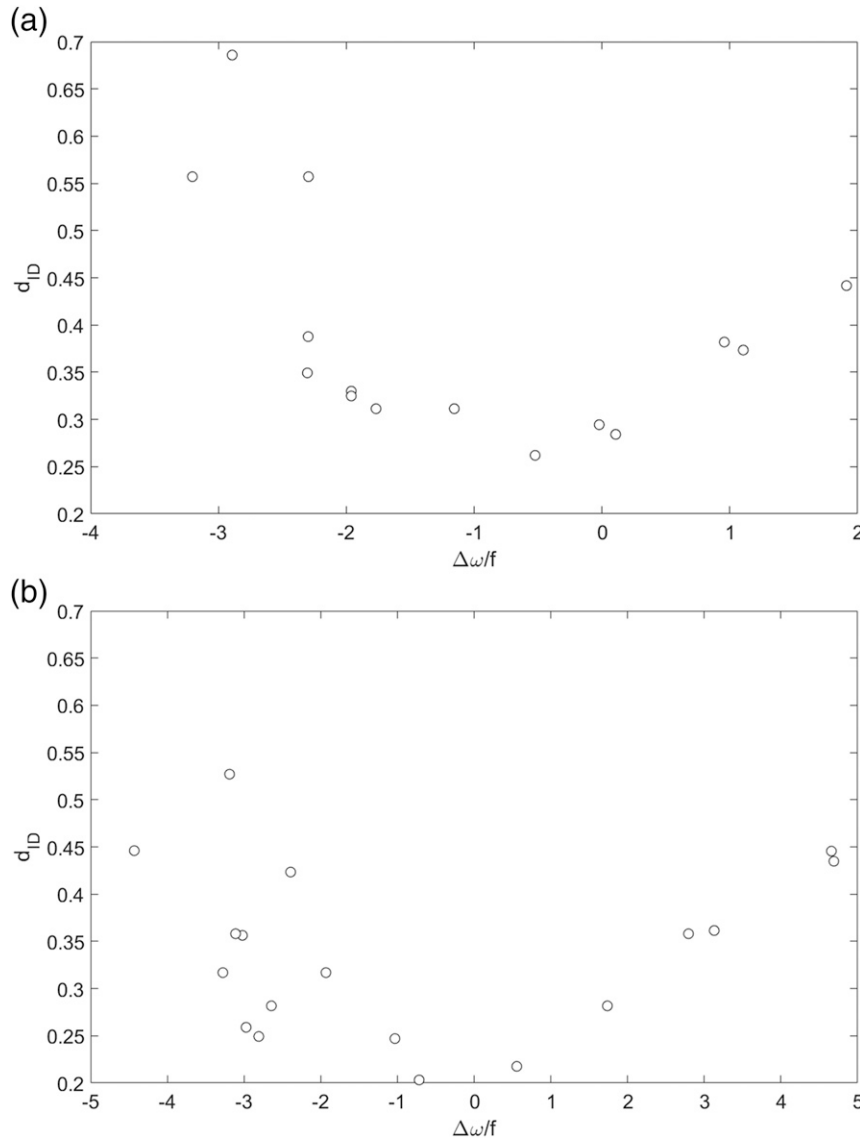
FIG. 14. The function $d_{ID}(\Delta\omega/f)$, where (a),(b) correspond to the interactions in Figs. 13a and 13b.

(McComas and Müller 1981b; Henyey et al. 1986; Gregg 1989; Polzin et al. 2014) can be applied to the output of high-resolution models, or improved through incorporation of the effect of variable spectral slopes. The latter is especially important due to the recent finding concerning the dependence of the downscale energy flux on the spectral slopes from numerical integrations of the kinetic equation (Eden et al. 2019b). To this end, we plan to develop systematic computations of the downscale energy cascade (with the resolution of its pathway in wavenumber–frequency space). The results can be compared to the microstructure observations in the ocean, potentially leading to an improved finescale parameterization for the estimation of the turbulent dissipation and diapycnal diffusivity.

Second, we are interested in the relation between the model grid resolution and the computed energy cascade. This requires numerical simulations with variable resolutions on the same region, and a theoretical consideration of the discrete wave turbulence (e.g., Kartashova 2007).

APPENDIX A

Derivation of the Interaction Coefficients

We start by the transformation of the Hamiltonian (15) from physical space to Fourier space, represented as the sum of a quadratic part and a cubic part:

$$H = H_{\text{quadratic}} + H_{\text{cubic}}, \tag{A1}$$

with

$$H_{\text{quadratic}} = \frac{1}{2} \int d\mathbf{p} \left\{ \frac{g}{N^2} k^2 |\phi_{\mathbf{p}}|^2 + \left(\frac{N^2 f^2}{gk^2} + \frac{g}{\rho_0^2 m^2} \right) |\Pi_{\mathbf{p}}'|^2 \right\}, \tag{a2}$$

$$H_{\text{cubic}} = \frac{1}{2} \int d\mathbf{p}\, d\mathbf{p}_1\, d\mathbf{p}_2 \delta_{\mathbf{p}+\mathbf{p}_1+\mathbf{p}_2} \left\{ \mathbf{k}_1 \cdot \mathbf{k}_2 \Pi' \phi_1 \phi_2 + \frac{N^4 f^2}{g^2} \frac{\mathbf{k}_1 \cdot \mathbf{k}_2}{k_1^2 k_2^2} \Pi' \Pi_1' \Pi_2' + 2 \frac{N^2 f}{g} \frac{\mathbf{k}_1 \cdot \mathbf{k}_2^{\perp}}{k_2^2} \Pi' \phi_1 \Pi_2' \right\}, \tag{A3}$$

where $\Pi' = \Pi - \Pi_0$, $\mathbf{k}^{\perp} = (-k_y, k_x)$, and we have used subscripts to denote the arguments of a function.

We then introduce the canonical variable $a_{\mathbf{p}}$ using (16), which allows the Hamiltonian structure expressed by the canonical form

$$i \frac{\partial}{\partial t} a_{\mathbf{p}} = \frac{\delta H}{\delta a_{\mathbf{p}}^*}, \tag{A4}$$

with $H = H_{\text{quadratic}} + H_{\text{cubic}}$ reduced to

$$H_{\text{quadratic}} = \int \omega_{\mathbf{p}} |a_{\mathbf{p}}|^2 \, d\mathbf{p} \tag{A5}$$

and

$$H_{\text{cubic}} = \int \left(V_{\mathbf{p}\mathbf{p}_1\mathbf{p}_2} a_{\mathbf{p}}^* a_{\mathbf{p}_1} a_{\mathbf{p}_2} + \text{C.C.} \right) \delta_{\mathbf{p}-\mathbf{p}_1-\mathbf{p}_2} \, d\mathbf{p}\, d\mathbf{p}_1\, d\mathbf{p}_2$$
$$+ \int \left(U_{\mathbf{p}\mathbf{p}_1\mathbf{p}_2} a_{\mathbf{p}}^* a_{\mathbf{p}_1}^* a_{\mathbf{p}_2}^* + \text{C.C.} \right) \delta_{\mathbf{p}+\mathbf{p}_1+\mathbf{p}_2} \, d\mathbf{p}\, d\mathbf{p}_1\, d\mathbf{p}_2, \tag{A6}$$

where C.C. represents the complex conjugate of the previous term.

To derive the interaction kernels V and U in (A6), we substitute (16) into (A3), and make use of the following properties of symmetry:

1) Integration sign symmetry: $\int_{-\infty}^{\infty} f(\mathbf{p}) \, d\mathbf{p} = \int_{-\infty}^{\infty} f(-\mathbf{p}) \, d\mathbf{p}$, to reverse the negative indices.
2) Integration variable symmetry: $\iint_{-\infty}^{\infty} f(\mathbf{p}_1, \mathbf{p}_2) \, d\mathbf{p}_1 \, d\mathbf{p}_2 = \iint_{-\infty}^{\infty} f(\mathbf{p}_2, \mathbf{p}_1) \, d\mathbf{p}_1 \, d\mathbf{p}_2$, to convert the delta function to the form in (A6).
3) Kernel symmetry: $V_{\mathbf{p}\mathbf{p}_1\mathbf{p}_2} = V_{\mathbf{p}\mathbf{p}_2\mathbf{p}_1}$, which allows the split of a function $f(\mathbf{p}, \mathbf{p}_1, \mathbf{p}_2) = [f(\mathbf{p}, \mathbf{p}_1, \mathbf{p}_2) + f(\mathbf{p}, \mathbf{p}_2, \mathbf{p}_1)]/2$.

More specifically, for the three terms in the integrand of (A3), we apply the properties 1 and 2 on both the first and second terms, and properties 1, 2, and 3 on the third term. This gives the final expressions of the kernel functions:

$$V_{\mathbf{p}\mathbf{p}_1\mathbf{p}_2} = \frac{N}{4\sqrt{2g}} \frac{1}{kk_1 k_2} \left(I_{\mathbf{p}\mathbf{p}_1\mathbf{p}_2} + J_{\mathbf{p},\mathbf{p}_1\mathbf{p}_2} + K_{\mathbf{p}\mathbf{p}_1\mathbf{p}_2} \right),$$

$$U_{\mathbf{p}\mathbf{p}_1\mathbf{p}_2} = \frac{N}{12\sqrt{2g}} \frac{1}{kk_1 k_2} \left(I_{\mathbf{p}\mathbf{p}_1\mathbf{p}_2} + J_{-\mathbf{p},\mathbf{p}_1\mathbf{p}_2} + K_{\mathbf{p}\mathbf{p}_1\mathbf{p}_2} \right),$$

$$I_{\mathbf{p}\mathbf{p}_1\mathbf{p}_2} = -\left(\sqrt{\frac{\omega_1 \omega_2}{\omega}} k^2 \mathbf{k}_1 \cdot \mathbf{k}_2 + \sqrt{\frac{\omega \omega_2}{\omega_1}} k_1^2 \mathbf{k} \cdot \mathbf{k}_2 + \sqrt{\frac{\omega_1 \omega}{\omega_2}} k_2^2 \mathbf{k}_1 \cdot \mathbf{k} \right),$$

$$J_{\mathbf{p},\mathbf{p}_1\mathbf{p}_2} = \frac{f^2}{\sqrt{\omega \omega_1 \omega_2}} \left(k^2 \mathbf{k}_1 \cdot \mathbf{k}_2 - k_1^2 \mathbf{k} \cdot \mathbf{k}_2 - k_2^2 \mathbf{k}_1 \cdot \mathbf{k} \right),$$

$$K_{\mathbf{p}\mathbf{p}_1\mathbf{p}_2} = if \left[\sqrt{\frac{\omega}{\omega_1 \omega_2}} (k_1^2 - k_2^2) \mathbf{k}_1 \cdot \mathbf{k}_2^{\perp} + \sqrt{\frac{\omega_1}{\omega_2 \omega}} (k_2^2 - k^2) \mathbf{k}_2 \cdot \mathbf{k}^{\perp} + \sqrt{\frac{\omega_2}{\omega \omega_1}} (k^2 - k_1^2) \mathbf{k} \cdot \mathbf{k}_1^{\perp} \right], \tag{A7}$$

where we have also used (1) in the derivation of $K_{\mathbf{pp}_1\mathbf{p}_2}$. The result presented here has a prefactor difference compared to Lvov and Tabak (2004), a sign difference compared to Lvov et al. (2010) (both for $K_{\mathbf{pp}_1\mathbf{p}_2}$), and is consistent with Lvov et al. (2012) which however only gives the form of $|V_{\mathbf{pp}_1\mathbf{p}_2}|^2$.

Equation (19) can then be derived by multiplying (A4) by $a_{\mathbf{p}}^*$, subtracting the complex conjugate of the result, and taking the ensemble average. The interaction with respect to the U kernel is neglected as a conventional approximation in WTT, due to the absence of the triad with $\omega + \omega_1 + \omega_2 = 0$.

APPENDIX B

Further Discussions on the Normalization in Bicoherence

We consider all motions in a progressive internal wave field associated with one frequency ω, i.e., $X(\mathbf{x}, z; \omega)e^{-i\omega t}$ with

$$X(\mathbf{x}, z; \omega) = \sum_{\left\{(\mathbf{k}_j, m_j)| k_j/m_j = \frac{\sqrt{\omega^2 - f^2}}{N}\right\}} A_j e^{i(\mathbf{k}_j \cdot \mathbf{x} + m_j z)}, \quad \text{(B1)}$$

where A_j is the modal amplitude, the condition $k_j/m_j = \sqrt{\omega^2 - f^2}/N$, resulted from dispersion relation (8), selects all wavenumber vector $\mathbf{p}_j = (\mathbf{k}_j, m_j)$ on a conical surface corresponding to frequency ω. We will use a simplified notation "j on ω" to represent $k_j/m_j = \sqrt{\omega^2 - f^2}/N$ hereafter. We will also neglect the A_j factor without loss of generality.

The temporal bicoherence (23) can now be written as

$$B(\omega_1, \omega_2) = \frac{\left| \left\langle \sum_{j \text{ on } \omega_1 + \omega_2} e^{i(-\mathbf{k}_j \cdot \mathbf{x} - m_j z)} \sum_{l \text{ on } \omega_1} e^{i(\mathbf{k}_l \cdot \mathbf{x} + m_l z)} \sum_{n \text{ on } \omega_2} e^{i(\mathbf{k}_n \cdot \mathbf{x} + m_n z)} \right\rangle^s \right|}{\left\langle \left| \sum_{j \text{ on } \omega_1 + \omega_2} e^{i(-\mathbf{k}_j \cdot \mathbf{x} - m_j z)} \right| \left| \sum_{l \text{ on } \omega_1} e^{i(\mathbf{k}_l \cdot \mathbf{x} + m_l z)} \right| \left| \sum_{n \text{ on } \omega_2} e^{i(\mathbf{k}_n \cdot \mathbf{x} + m_n z)} \right| \right\rangle^s}. \quad \text{(B2)}$$

For the numerator, after the spatial average on $(\mathbf{x}, z)$, the only surviving terms are those with $\mathbf{p}_l + \mathbf{p}_n = \mathbf{p}_j$, i.e., the triads of resonant interactions. Therefore, the numerator can be viewed as $\sum_{(j,l,n)|\mathbf{p}_l + \mathbf{p}_n = \mathbf{p}_j} [E(\omega_1 + \omega_2, k_j) E(\omega_1, k_l) E(\omega_2, k_n)]^{1/2}$. For the denominator, the modulus are taken before the multiplications, leading to $[E(\omega_1 + \omega_2) E(\omega_1) E(\omega_2)]^{1/2}$. It is clear that the denominator *can* be much larger than the numerator (which is indeed the case for a GM-like spectrum), since the condition $\mathbf{p}_l + \mathbf{p}_n = \mathbf{p}_j$ only selects a small subset of all modes on the cone surface. This results in $B(\omega_1, \omega_2) \ll 1$, i.e., the normalization in (23) does not lead to an $O(1)$ quantity.

On the other hand, the normalization issue does not exist in (24), since one vector wavenumber corresponds to only one frequency (or one wave mode). Therefore $B(\mathbf{p}_1, \mathbf{p}_2) \sim O(1)$, which has been confirmed in our numerical analysis.

REFERENCES

Alford, M., J. MacKinnon, Z. Zhao, R. Pinkel, J. Klymak, and T. Peacock, 2007: Internal waves across the Pacific. *Geophys. Res. Lett.*, **34**, L24601, https://doi.org/10.1029/2007GL031566.

Ansong, J. K., B. K. Arbic, M. C. Buijsman, J. G. Richman, J. F. Shriver, and A. J. Wallcraft, 2015: Indirect evidence for substantial damping of low-mode internal tides in the open ocean. *J. Geophys. Res. Oceans*, **120**, 6057–6071, https://doi.org/10.1002/2015JC010998.

Arbic, B. K., and Coauthors, 2018: Primer on global internal tide and internal gravity wave continuum modeling in HYCOM and MITgcm. *New Frontiers in Operational Oceanography*, E. P. Chassignet et al., Eds., GODAE OceanView, 307–392.

Barkan, R., K. B. Winters, and J. C. McWilliams, 2017: Stimulated imbalance and the enhancement of eddy kinetic energy dissipation by internal waves. *J. Phys. Oceanogr.*, **47**, 181–198, https://doi.org/10.1175/JPO-D-16-0117.1.

Briscoe, M. G., 1977: Gaussianity of internal waves. *J. Geophys. Res.*, **82**, 2117–2126, https://doi.org/10.1029/JC082i015p02117.

Cairns, J. L., and G. O. Williams, 1976: Internal wave observations from a midwater float, 2. *J. Geophys. Res.*, **81**, 1943–1950, https://doi.org/10.1029/JC081i012p01943.

Chen, Z., S. Chen, Z. Liu, J. Xu, J. Xie, Y. He, and S. Cai, 2019: Can tidal forcing alone generate a GM-like internal wave spectrum? *Geophys. Res. Lett.*, **46**, 14 644–14 652, https://doi.org/10.1029/2019GL086338.

Cushman-Roisin, B., and J.-M. Beckers, 2011: *Physical and Numerical Aspects*. 2nd ed. Introduction to Geophysical Fluid Dynamics, Vol. 101. Academic Press, 875 pp.

Daru, V., and C. Tenaud, 2004: High order one-step monotonicity-preserving schemes for unsteady compressible flow calculations. *J. Comput. Phys.*, **193**, 563–594, https://doi.org/10.1016/j.jcp.2003.08.023.

Eden, C., M. Chouksey, and D. Olbers, 2019a: Mixed Rossby–gravity wave–wave interactions. *J. Phys. Oceanogr.*, **49**, 291–308, https://doi.org/10.1175/JPO-D-18-0074.1.

——, F. Pollmann, and D. Olbers, 2019b: Numerical evaluation of energy transfers in internal gravity wave spectra of the ocean. *J. Phys. Oceanogr.*, **49**, 737–749, https://doi.org/10.1175/JPO-D-18-0075.1.

——, ——, and ——, 2020: Towards a global spectral energy budget for internal gravity waves in the ocean. *J. Phys. Oceanogr.*, **50**, 935–944, https://doi.org/10.1175/JPO-D-19-0022.1.

Fox-Kemper, B., and D. Menemenlis, 2008: Can large eddy simulation techniques improve mesoscale rich ocean models? *Ocean Modeling in an Eddying Regime, Geophys. Monogr.*, Vol. **177**, Amer. Geophys. Union, 319–337, https://doi.org/10.1029/177GM19.

Furue, R., 2003: Energy transfer within the small-scale oceanic internal wave spectrum. *J. Phys. Oceanogr.*, **33**, 267–282, https://doi.org/10.1175/1520-0485(2003)033<0267:ETWTSS>2.0.CO;2.

Furuichi, N., T. Hibiya, and Y. Niwa, 2005: Bispectral analysis of energy transfer within the two-dimensional oceanic internal wave field. *J. Phys. Oceanogr.*, **35**, 2104–2109, https://doi.org/10.1175/JPO2816.1.

Gargett, A., 1984: Vertical eddy diffusivity in the ocean interior. *J. Mar. Res.*, **42**, 359–393, https://doi.org/10.1357/002224084788502756.

Garrett, C., and W. Munk, 1972: Space-time scales of internal waves. *Geophys. Astrophys. Fluid Dyn.*, **3**, 225–264, https://doi.org/10.1080/03091927208236082.

——, and ——, 1975: Space-time scales of internal waves: A progress report. *J. Geophys. Res.*, **80**, 291–297, https://doi.org/10.1029/JC080i003p00291.

Gregg, M., 1989: Scaling turbulent dissipation in the thermocline. *J. Geophys. Res.*, **94**, 9686–9698, https://doi.org/10.1029/JC094iC07p09686.

Hasselmann, K., 1962: On the non-linear energy transfer in a gravity-wave spectrum Part 1. General theory. *J. Fluid Mech.*, **12**, 481–500, https://doi.org/10.1017/S0022112062000373.

Haubrich, R. A., 1965: Earth noise, 5 to 500 millicycles per second: 1. Spectral stationarity, normality, and nonlinearity. *J. Geophys. Res.*, **70**, 1415–1427, https://doi.org/10.1029/JZ070i006p01415.

Henyey, F. S., J. Wright, and S. M. Flatté, 1986: Energy and action flow through the internal wave field: An eikonal approach. *J. Geophys. Res.*, **91**, 8487–8495, https://doi.org/10.1029/JC091iC07p08487.

Hibiya, T., Y. Niwa, and K. Fujiwara, 1998: Numerical experiments of nonlinear energy transfer within the oceanic internal wave spectrum. *J. Geophys. Res.*, **103**, 18 715–18 722, https://doi.org/10.1029/98JC01362.

——, M. Nagasawa, and Y. Niwa, 2002: Nonlinear energy transfer within the oceanic internal wave spectrum at mid and high latitudes. *J. Geophys. Res.*, **107**, 3207, https://doi.org/10.1029/2001JC001210.

Kartashova, E., 2007: Exact and quasiresonances in discrete water wave turbulence. *Phys. Rev. Lett.*, **98**, 214502, https://doi.org/10.1103/PhysRevLett.98.214502.

Large, W. G., J. C. McWilliams, and S. C. Doney, 1994: Oceanic vertical mixing: A review and a model with a nonlocal boundary layer parameterization. *Rev. Geophys.*, **32**, 363–403, https://doi.org/10.1029/94RG01872.

Leaman, K. D., and T. B. Sanford, 1975: Vertical energy propagation of inertial waves: A vector spectral analysis of velocity profiles. *J. Geophys. Res.*, **80**, 1975–1978, https://doi.org/10.1029/JC080i015p01975.

Levine, M. D., J. D. Irish, T. E. Ewart, and S. A. Reynolds, 1986: Simultaneous spatial and temporal measurements of the internal wave field during mate. *J. Geophys. Res.*, **91**, 9709–9719, https://doi.org/10.1029/JC091iC08p09709.

Lvov, Y. V., and E. G. Tabak, 2001: Hamiltonian formalism and the Garrett-Munk spectrum of internal waves in the ocean. *Phys. Rev. Lett.*, **87**, 168501, https://doi.org/10.1103/PhysRevLett.87.168501.

——, and ——, 2004: A Hamiltonian formulation for long internal waves. *Physica D*, **195**, 106–122, https://doi.org/10.1016/j.physd.2004.03.010.

——, K. L. Polzin, and E. G. Tabak, 2004: Energy spectra of the ocean's internal wave field: Theory and observations. *Phys. Rev. Lett.*, **92**, 128501, https://doi.org/10.1103/physrevlett.92.128501.

——, ——, ——, and N. Yokoyama, 2010: Oceanic internal-wave field: Theory of scale-invariant spectra. *J. Phys. Oceanogr.*, **40**, 2605–2623, https://doi.org/10.1175/2010JPO4132.1.

——, ——, and N. Yokoyama, 2012: Resonant and near-resonant internal wave interactions. *J. Phys. Oceanogr.*, **42**, 669–691, https://doi.org/10.1175/2011JPO4129.1.

MacKinnon, J. A., and Coauthors, 2017: Climate process team on internal wave–driven ocean mixing. *Bull. Amer. Meteor. Soc.*, **98**, 2429–2454, https://doi.org/10.1175/BAMS-D-16-0030.1.

Marshall, J., C. Hill, L. Perelman, and A. Adcroft, 1997: Hydrostatic, quasi-hydrostatic, and nonhydrostatic ocean modeling. *J. Geophys. Res.*, **102**, 5733–5752, https://doi.org/10.1029/96JC02776.

McComas, C. H., and F. P. Bretherton, 1977: Resonant interaction of oceanic internal waves. *J. Geophys. Res.*, **82**, 1397–1412, https://doi.org/10.1029/JC082i009p01397.

——, and M. G. Briscoe, 1980: Bispectra of internal waves. *J. Fluid Mech.*, **97**, 205–213, https://doi.org/10.1017/S0022112080002510.

——, and P. Müller, 1981a: The dynamic balance of internal waves. *J. Phys. Oceanogr.*, **11**, 970–986, https://doi.org/10.1175/1520-0485(1981)011<0970:TDBOIW>2.0.CO;2.

——, and ——, 1981b: Time scales of resonant interactions among oceanic internal waves. *J. Phys. Oceanogr.*, **11**, 139–147, https://doi.org/10.1175/1520-0485(1981)011<0139:TSORIA>2.0.CO;2.

Müller, M., B. K. Arbic, J. G. Richman, J. F. Shriver, E. L. Kunze, R. B. Scott, A. J. Wallcraft, and L. Zamudio, 2015: Toward an internal gravity wave spectrum in global ocean models. *Geophys. Res. Lett.*, **42**, 3474–3481, https://doi.org/10.1002/2015GL063365.

Müller, P., D. Olbers, and J. Willebrand, 1978: The Iwex spectrum. *J. Geophys. Res.*, **83**, 479–500, https://doi.org/10.1029/JC083iC01p00479.

——, G. Holloway, F. Henyey, and N. Pomphrey, 1986: Nonlinear interactions among internal gravity waves. *Rev. Geophys.*, **24**, 493–536, https://doi.org/10.1029/RG024i003p00493.

Munk, W., and C. Wunsch, 1998: Abyssal recipes II: Energetics of tidal and wind mixing. *Deep-Sea Res. I*, **45**, 1977–2010, https://doi.org/10.1016/S0967-0637(98)00070-3.

Nazarenko, S., 2011: *Wave Turbulence*. Lecture Notes in Physics, Vol. 825. Springer, 279 pp.

Nelson, A. D., B. K. Arbic, D. Menemenlis, W. R. Peltier, N. Grisouard, and J. Klymak, 2020: Improved internal wave spectral continuum in a regional ocean model. *J. Geophys. Res. Oceans*, **125**, e2019JC015974, https://doi.org/10.1029/2019JC015974.

Olbers, D. J., 1976: Nonlinear energy transfer and the energy balance of the internal wave field in the deep ocean. *J. Fluid Mech.*, **74**, 375–399, https://doi.org/10.1017/S0022112076001857.

——, F. Pollmann, and C. Eden, 2020: On PSI interactions in internal gravity wave fields and the decay of baroclinic tides. *J. Phys. Oceanogr.*, **50**, 751–771, https://doi.org/10.1175/JPO-D-19-0224.1.

Onuki, Y., and T. Hibiya, 2018: Decay rates of internal tides estimated by an improved wave–wave interaction analysis. *J. Phys. Oceanogr.*, **48**, 2689–2701, https://doi.org/10.1175/JPO-D-17-0278.1.

Pan, Y., and D. K. Yue, 2014: Direct numerical investigation of turbulence of capillary waves. *Phys. Rev. Lett.*, **113**, 094501, https://doi.org/10.1103/PhysRevLett.113.094501.

Pelinovsky, E. N., and M. Raevsky, 1977: Weak turbulence of the internal waves of the ocean. *Izv. Acad. Sci. USSR Atmos. Oceanic Phys.*, **13**, 187–193.

Polzin, K. L., and Y. V. Lvov, 2011: Toward regional characterizations of the oceanic internal wavefield. *Rev. Geophys.*, **49**, RG4003, https://doi.org/10.1029/2010RG000329.

——, A. C. N. Garabato, T. N. Huussen, B. M. Sloyan, and S. Waterman, 2014: Finescale parameterizations of turbulent dissipation. *J. Geophys. Res. Oceans*, **119**, 1383–1419, https://doi.org/10.1002/2013JC008979.

Ponce, M., and Coauthors, 2019: Deploying a top-100 supercomputer for large parallel workloads: The Niagara supercomputer. *Proc. Practice and Experience in Advanced Research Computing on Rise of the Machines (Learning)*, Chicago, IL, ACM, 34, https://doi.org/10.1145/3332186.3332195.

Riley, J. J., and M.-P. Lelong, 2000: Fluid motions in the presence of strong stable stratification. *Annu. Rev. Fluid Mech.*, **32**, 613–657, https://doi.org/10.1146/annurev.fluid.32.1.613.

Rocha, C. B., T. K. Chereskin, S. T. Gille, and D. Menemenlis, 2016: Mesoscale to submesoscale wavenumber spectra in Drake Passage. *J. Phys. Oceanogr.*, **46**, 601–620, https://doi.org/10.1175/JPO-D-15-0087.1.

Shriver, J., B. K. Arbic, J. Richman, R. Ray, E. Metzger, A. Wallcraft, and P. Timko, 2012: An evaluation of the barotropic and internal tides in a high-resolution global ocean circulation model. *J. Geophys. Res.*, **117**, C10024, https://doi.org/10.1029/2012JC008170.

Simmons, H. L., and M. H. Alford, 2012: Simulating the long-range swell of internal waves generated by ocean storms. *Oceanography*, **25**, 30–41, https://doi.org/10.5670/oceanog.2012.39.

——, R. W. Hallberg, and B. K. Arbic, 2004: Internal wave generation in a global baroclinic tide model. *Deep-Sea Res. II*, **51**, 3043–3068, https://doi.org/10.1016/j.dsr2.2004.09.015.

Sugiyama, Y., Y. Niwa, and T. Hibiya, 2009: Numerically reproduced internal wave spectra in the deep ocean. *Geophys. Res. Lett.*, **36**, L07601, https://doi.org/10.1029/2008GL036825.

Sun, O. M., and R. Pinkel, 2012: Energy transfer from high-shear, low-frequency internal waves to high-frequency waves near Kaena Ridge, Hawaii. *J. Phys. Oceanogr.*, **42**, 1524–1547, https://doi.org/10.1175/JPO-D-11-0117.1.

Thong, T., J. McNames, and M. Aboy, 2004: Lomb-Wech periodogram for non-uniform sampling. *26th Annual Int. Conf. of the IEEE Engineering in Medicine and Biology Society*, San Francisco, CA, IEEE, 271–274, https://doi.org/10.1109/IEMBS.2004.1403144.

Voronovich, A. G., 1979: Hamiltonian formalism for internal waves in the ocean. *Izv. Atmos. Ocean. Phys.*, **16**, 52–57.

Zakharov, V. E., and N. Filonenko, 1966: Energy spectrum for stochastic oscillations of the surface of a liquid. *Dokl. Akad. Nauk SSSR*, **170**, 1292–1295.

——, V. S. L'vov, and G. Falkovich, 1992: *Kolmogorov Spectra of Turbulence 1. Wave Turbulence*. Springer, 275 pp.

Zhao, Z., M. H. Alford, J. A. MacKinnon, and R. Pinkel, 2010: Long-range propagation of the semidiurnal internal tide from the Hawaiian ridge. *J. Phys. Oceanogr.*, **40**, 713–736, https://doi.org/10.1175/2009JPO4207.1.